

A mitochondrial surveillance mechanism activated by *SRSF2* mutations in hematologic malignancies

Xiaolei Liu,¹ Sudhish A. Devadiga,¹ Robert F. Stanley,² Ryan M. Morrow,³ Kevin A. Janssen,³ Mathieu Quesnel-Vallières,⁴ Oz Pomp,⁵ Adam A. Moverley,⁵ Chenchen Li,¹ Nicolas Skuli,¹ Martin Carroll,¹ Jian Huang,⁶ Douglas C. Wallace,^{3,7} Kristen W. Lynch,⁴ Omar Abdel-Wahab,² and Peter S. Klein^{1,5}

¹Department of Medicine, Division of Hematology-Oncology, Perelman School of Medicine, University of Pennsylvania, Philadelphia, Pennsylvania, USA. ²Molecular Pharmacology Program, Sloan Kettering Institute, Memorial Sloan Kettering Cancer Center, New York, New York, USA. ³Center for Mitochondrial and Epigenomic Medicine, Children's Hospital of Philadelphia, Philadelphia, Pennsylvania, USA. ⁴Department of Biochemistry and Biophysics and ⁵Department of Cell and Developmental Biology, Institute for Regenerative Medicine, Perelman School of Medicine, University of Pennsylvania, Philadelphia, Pennsylvania, USA. ⁶Coriell Institute for Medical Research, Camden, New Jersey, USA. ⁷Department of Pediatrics, Division of Human Genetics, Perelman School of Medicine, University of Pennsylvania, Philadelphia, Pennsylvania, USA.

Splicing factor mutations are common in myelodysplastic syndrome (MDS) and acute myeloid leukemia (AML), but how they alter cellular functions is unclear. We show that the pathogenic *SRSF2*^{P95H/+} mutation disrupts the splicing of mitochondrial mRNAs, impairs mitochondrial complex I function, and robustly increases mitophagy. We also identified a mitochondrial surveillance mechanism by which mitochondrial dysfunction modifies splicing of the mitophagy activator *PINK1* to remove a poison intron, increasing the stability and abundance of *PINK1* mRNA and protein. *SRSF2*^{P95H}-induced mitochondrial dysfunction increased *PINK1* expression through this mechanism, which is essential for survival of *SRSF2*^{P95H/+} cells. Inhibition of splicing with a glycogen synthase kinase 3 inhibitor promoted retention of the poison intron, impairing mitophagy and activating apoptosis in *SRSF2*^{P95H/+} cells. These data reveal a homeostatic mechanism for sensing mitochondrial stress through *PINK1* splicing and identify increased mitophagy as a disease marker and a therapeutic vulnerability in *SRSF2*^{P95H} mutant MDS and AML.

Introduction

Myelodysplastic syndrome (MDS) is a clonal hematopoietic disorder characterized by hyperproliferative bone marrow, dysplastic hematopoietic cells, peripheral cytopenias, and high risk of progression to acute myeloid leukemia (AML). Recurrent mutations in RNA splicing factors, including *SF3B1*, *SRSF2*, and *U2AF1*, account for 60%–70% of somatic mutations in MDS (1) and are common in myeloproliferative neoplasms (MPNs), the MDS/MPN overlap disorder chronic myelomonocytic leukemia (CMML), and AML (1–6). However, the mechanisms by which these mutations alter cellular functions or contribute to transformation remain unclear.

Mutations in distinct splicing factors cause myeloid disorders with similar phenotypic features but limited overlap in specific mRNAs that are aberrantly spliced. This may suggest that distinct mRNA targets are responsible for these myeloid malignancies

or that shared pathways are affected downstream of aberrantly spliced mRNAs. Hotspot mutations in *SRSF2* alter RNA binding site specificity and disrupt the splicing of mRNAs encoding hematopoietic regulators that are frequently mutated in AML (7, 8). For example, the *SRSF2*^{P95*} mutation promotes inclusion of a poison exon in *EZH2* mRNA, leading to nonsense-mediated decay and reduced levels of *EZH2* (7). Thus, the number of patients with reduced *EZH2* expression is higher than the number with *EZH2* mutations (8). These studies support a pathogenic mechanism targeting the splicing of a single mRNA, but do not rule out additional contributions from other splicing events. Furthermore, transcriptomic analyses of different splicing factor mutants show that altered splicing of distinct mRNAs can affect common downstream pathways, including splicing itself, protein synthesis, and mitochondrial function (9).

Splicing factor mutations occur as mutually exclusive, heterozygous point mutations at specific residues (10, 11). The presence of a wild-type splicing factor is required for survival of MDS cells that express a mutant splicing factor, suggesting vulnerability associated with disrupted splicing factor activity. Consistent with this, hematopoietic cells with heterozygous splicing factor mutations are sensitized to additional perturbation of the splicing machinery by small-molecule splicing inhibitors (12, 13). This observation has led to clinical trials with splicing inhibitors in refractory leukemia patients (12, 14–18). However, these trials have been ineffective so far (14), and there are currently no FDA-approved therapies that target splicing factors in MDS or AML.

Conflict of interest: PSK is collaborating with Blueprint Medicines under a sponsored research agreement. OAW has served as a consultant for H3B Biomedicine, Foundation Medicine Inc., Merck, Prelude Therapeutics, and Janssen, and is on the Scientific Advisory Board of Envisagenics Inc., AlChem, Harmonic Discovery Inc., and Pfizer Boulder. OAW has received prior research funding from H3B Biomedicine, Nurix Therapeutics, Minovia Therapeutics, and LOXO Oncology. DCW is on the Scientific Advisory Boards of Pano Therapeutics and Medical Excellence Capital.

Copyright: © 2024, Liu et al. This is an open access article published under the terms of the Creative Commons Attribution 4.0 International License.

Submitted: September 11, 2023; **Accepted:** April 25, 2024; **Published:** May 7, 2024.

Reference information: *J Clin Invest.* 2024;134(12):e175619.

<https://doi.org/10.1172/JCI175619>.

Glycogen synthase kinase-3 α (GSK-3 α) and GSK-3 β are multi-functional serine/threonine kinases encoded by 2 similar genes, *GSK3A* and *GSK3B*. GSK-3 functions downstream of Flt3, c-Kit, and Wnt signaling, all pathways associated with MDS and AML (19). *Gsk3a/b* knockdown (20) or *Gsk3b* deletion (21) in mouse bone marrow causes a pronounced myeloproliferative phenotype, and *Gsk3a/b* double-knockout (DKO) causes marked expansion of both mature granulocytes and primitive blasts, leading to an aggressive AML (21), but the substrates that mediate GSK-3 functions in mouse and human hematopoietic malignancies have not been extensively characterized. Our recent phosphoproteomic analysis of GSK-3 substrates identified multiple core splicing factors implicated in MDS and AML (19, 22), consistent with prior studies supporting the importance of GSK-3 in splicing regulation, including evidence that GSK-3 phosphorylation of SRSF2 regulates splicing of *MAPT* (Tau) exon 10 (23–25). Both pharmacologic inhibition and genetic loss of *GSK3* disrupt pre-mRNA splicing on a transcriptome-wide scale in diverse cell types (19, 26), raising the possibility that clinically well tolerated GSK-3 inhibitors could be repurposed to treat splicing factor mutant MDS and AML.

In the present study, we assessed transcriptome-wide changes in splicing upon GSK-3 inhibition (GSK-3i) in leukemic cells. We find that GSK-3i disrupts splicing and selectively kills MDS and AML cells with splicing factor mutations. Mechanistically, GSK-3i induces a heightened splicing response in splicing factor mutant cells by repressing cassette exon inclusion and promoting intron retention. These findings led us to focus on SRSF2, as *SRSF2*-mutant cells show disrupted splicing of nuclear-encoded mitochondrial genes, impaired mitochondrial function, and an increase in mitophagy that is essential for their survival. Splicing of mRNA encoding the mitochondrial surveillance factor *PINK1* is altered in response to mitochondrial stress in *SRSF2*^{P95H/+} mutant cells, leading to a more stable splice form and reflecting what we believe to be a novel mechanism for sensing mitochondrial stress. GSK-3i disrupts splicing of *PINK1*, promoting a splice form with a premature stop codon and reducing overall *PINK1* mRNA levels. The reduction in *PINK1* is associated with reduced mitophagy and enhanced cell death in *SRSF2*^{P95H/+} mutant cells, sparing cells with wild-type *SRSF2*. Our findings reveal a mechanism for mitochondrial surveillance and identify a new therapeutic vulnerability in *SRSF2*-mutant MDS and AML.

Results

Preferential sensitivity of spliceosomal mutant leukemia to GSK-3i. Heterozygous splicing factor mutations sensitize leukemic cells to additional perturbation of the core splicing machinery (13). As GSK-3 regulates splicing in other cell types (22–26), we tested whether GSK-3i would enhance cell death in leukemic cells with heterozygous knockins of recurrent driver mutations in *SRSF2* and *SF3B1*. Isogenic *SRSF2*^{P95H/+} and *SF3B1*^{K700E/+} knockin K562 cells (13) were cultured with the GSK-3 inhibitor CHIR99021 (CHIR) or vehicle control, and proliferation was monitored at 2 and 4 days. Both *SRSF2*^{P95H/+} and *SF3B1*^{K700E/+} cells were preferentially sensitive to CHIR (Figure 1A and Supplemental Figure 1A; supplemental material available online with this article; <https://doi.org/10.1172/JCI1175619DS1>) and the clinically well-tolerated GSK-3 inhibitor lithium (Supplemental Figure 1B) compared with isogenic cells with wild-type (WT), *SRSF2*, and *SF3B1*. A flow cytometric assay

for apoptosis revealed that GSK-3i promoted both early and late apoptosis (Figure 1B) in splicing factor mutant cells compared with parental cells but had little impact on their cell cycle status (Supplemental Figure 1C). Collectively, these data demonstrate that GSK-3i preferentially kills spliceosomal mutant leukemias.

As an alternative approach to compare the effect of mutated and WT *SRSF2* in otherwise genetically identical cells, we introduced *SRSF2*^{P95H} or *SRSF2*^{WT} into parental TF-1 or K562 cells along with mCherry (Supplemental Figure 1, D and E), and then followed proliferation of mCherry-positive and untransduced cells. Expression of *SRSF2*^{P95H} resulted in a competitive disadvantage in comparison with WT-expressing cells (Supplemental Figure 1F), consistent with prior reports (7, 27). Further, GSK-3i markedly increased apoptosis in TF-1 and K562 cells expressing *SRSF2*^{P95H} compared with parental cells and cells overexpressing *SRSF2*^{WT} (Figure 1C and Supplemental Figure 1G). Therefore, *SRSF2*^{P95H} confers sensitivity to GSK-3i whether introduced as a heterozygous knockin or overexpressed in a genetically identical background.

We next tested whether GSK-3i selectively kills splicing factor mutant cells in vivo in mice bearing xenografts of isogenic WT and *SRSF2*^{P95H/+} K562 cells (Figure 1D). Daily administration of CHIR slowed the growth of xenografts with *SRSF2*^{P95H/+} ($P = 0.0036$) but had no significant effect on *SRSF2*^{WT} xenografts (Figure 1E and Supplemental Figure 1, H and I).

GSK-3i induces cell death in splicing factor mutant cells from patients with hematologic malignancies. Based on the promising results with leukemic cell lines (Figure 1), we evaluated the preferential cytotoxicity of GSK-3i in primary cells from patients with AML or the MDS/MPN overlap disorder CMML. GSK-3i induced apoptosis in primary cells from patients with CMML or AML with *SRSF2*, *SF3B1*, or *U2AF1* mutations, but not in leukemic cells with WT splicing factors or in CD34⁺ cells from healthy subjects (Figure 2A and Supplemental Table 1).

Given the heterogeneity of primary human AML cells, we also tested the preferential cytotoxicity of GSK-3i in an isogenic context by expressing *SRSF2*^{WT} or *SRSF2*^{P95H} with mCherry in primary blasts from AML patients with WT splicing factors and then assessing the loss of mCherry-positive cells over time with or without CHIR treatment (Figure 2B and Supplemental Table 1). Primary AML cells expressing *SRSF2*^{P95H} were preferentially depleted upon CHIR exposure (Figure 2C). In contrast, GSK-3i had no substantial effect on primary AML cells expressing WT *SRSF2* (Figure 2C). Cells expressing mutant *SRSF2* also displayed a higher level of apoptosis in response to CHIR treatment relative to controls transduced with WT *SRSF2* (Figure 2D and Supplemental Figure 2). These data confirm that *SRSF2*^{P95H} confers sensitivity to GSK-3i in primary AML cells.

GSK-3i alters global gene expression and splicing in human leukemic cells. To understand the functional consequences of GSK-3i for gene expression and splicing, we performed deep RNA sequencing (RNA-Seq; 10⁸ reads per replicate sample) of parental K562 and isogenic *SRSF2*^{P95H/+} and *SF3B1*^{K700E/+} lines treated with or without CHIR (Figure 3A and Supplemental Figure 3). CHIR treatment had distinct effects on the transcriptomes of WT, *SRSF2*^{P95H/+}, and *SF3B1*^{K700E/+} mutant cells (Supplemental Figure 3, B and C, and Supplemental Table 2). Additionally, GSK-3i altered the expression of multiple *BCL2* family genes in a manner that may contribute to cell death, including decreased expression of the antiapoptotic

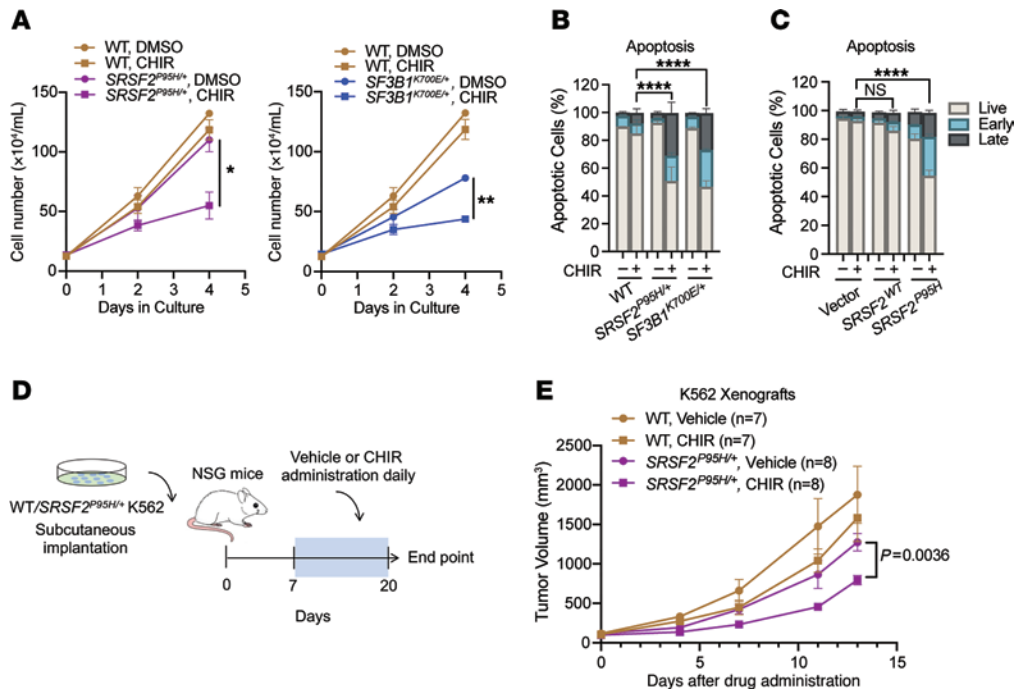


Figure 1. Preferential cytotoxicity of GSK-3i in splicing factor mutant leukemia over WT counterparts. (A) WT, *SRSF2*^{P95H/+}, and *SF3B1*^{K700E/+} cells were cultured with DMSO or 3 μM CHIR, and cell numbers were counted at 2 and 4 days (mean ± SD). (B) Percentages of viable and early- and late-apoptotic cells based on 7-AAD and annexin V flow cytometric analysis of isogenic K562 WT, *SRSF2*^{P95H/+}, and *SF3B1*^{K700E/+} cells treated with DMSO or 3 μM CHIR in vitro for 4 days (mean ± SD). Statistical analysis of viable fraction in mutant cells treated with CHIR relative to WT counterparts was performed using a 2-tailed χ^2 test. *****P* < 0.0001. (C) Percentages of viable and early- and late-apoptotic cells of K562 parental or *SRSF2*^{WT}- or *SRSF2*^{P95H}-overexpressing cells treated with vehicle or 3 μM CHIR in vitro for 4 days (mean ± SD). Statistical analysis of viable fraction in *SRSF2*^{P95H}-overexpressing cells treated with CHIR relative to *SRSF2*^{WT} counterparts was performed using a 2-tailed χ^2 test. *****P* < 0.0001. (D) Schematic of in vivo K562 xenograft experiment. (E) Mean tumor volume in NSG mice subcutaneously implanted with K562 isogenic WT or *SRSF2*^{P95H/+} cells. Mice received subcutaneous injections of vehicle or CHIR (30 mg/kg) daily. Mean tumor volumes ± SEM are shown. For data in A and E, **P* < 0.05 and ***P* < 0.01 (2-way ANOVA with Šidák's multiple-comparison test).

BCL-xL (encoded by *BCL2L1*) and increased expression of the pro-apoptotic genes *BAK1*, *BCL2L11*, and *BIK* regardless of splicing factor mutation status (Supplemental Figure 3D).

We then performed genome-wide analysis of splicing using the rMATS pipeline (28). We measured the change in percentage spliced in (Δ PSI or dPSI) values across 5 main types of alternative splicing events (skipped exon, alternative 5' splice site exon, alternative 3' splice site exon, mutually exclusive exons, and retained introns) in CHIR-treated versus control cells (Supplemental Table 3). Using a false discovery rate (FDR) less than 0.05 and dPSI greater than 10% (Figure 3B), we identified 694 alternative splicing events in parental cells, 705 in *SRSF2*^{P95H/+} cells, and 872 in *SF3B1*^{K700E/+} cells. However, only 32 differentially spliced mRNAs were found in all 3 genotypes upon GSK-3i, suggesting that GSK-3i has distinct and independent consequences for splicing in WT and splicing factor mutant cells (Figure 3, C and D). The predominant change in RNA splicing upon CHIR treatment in *SRSF2*^{P95H/+} and *SF3B1*^{K700E/+} cells was increased cassette exon skipping relative to DMSO-treated controls, while approximately equal proportions of exon inclusion and exclusion with CHIR exposure were observed in parental cells (Figure 3E). *SF3B1* normally facilitates 3' splice site recognition and is involved in the splicing of most introns by binding to the branchpoint (29). GSK-3i in *SF3B1*^{K700E/+} cells resulted in a higher proportion of repressed alternative 3' splice site (Figure 3F) and an increased number of retained intron events (Figure 3B). Consistent with the distinct effects of GSK-3i on splicing in

cells with WT versus mutant splicing factors, multiple regulators of hematopoietic cell survival and proliferation were alternatively spliced only in splicing factor mutant K562 cells (Figure 3G and Supplemental Figure 3E). Among them, GSK-3i enhanced exon skipping in *DEPDC1* pre-mRNA in *SRSF2*^{P95H/+} cells compared with WT counterparts, an event that was further validated by transcript-specific quantitative reverse transcriptase PCR (RT-qPCR) (Figure 3G). Taken together, these data show that inhibition of GSK-3 further reduces splicing fidelity in splicing factor mutant hematopoietic cells, likely explaining the selective toxicity of GSK-3i to splicing factor mutant leukemias over WT counterparts.

GSK-3 regulates PINK1 splicing. To test whether genes that are alternatively spliced following GSK-3i contribute to the preferential killing of spliceosome-mutant cells, we evaluated transcripts that exhibit concomitant dysregulation in gene expression and splicing with CHIR treatment (Figure 4A). We focused our attention initially on *PINK1*, because it is a serine/threonine kinase that serves as a critical sensor of mitochondrial damage and activates mitophagy to maintain mitochondrial homeostasis (30). GSK-3i reduces the abundance and alters the splicing of *PINK1* mRNA in WT, *SRSF2*^{P95H/+}, and *SF3B1*^{K700E/+} K562 cells. A sashimi plot shows that GSK-3i enhances the retention of intron 6, which includes a premature termination codon (PTC) that is predicted to promote mRNA degradation through nonsense-mediated decay (NMD) (Figure 4B). RT-qPCR confirms that GSK-3i reduces the abundance of *PINK1* in WT, *SRSF2*^{P95H/+}, and *SF3B1*^{K700E/+}

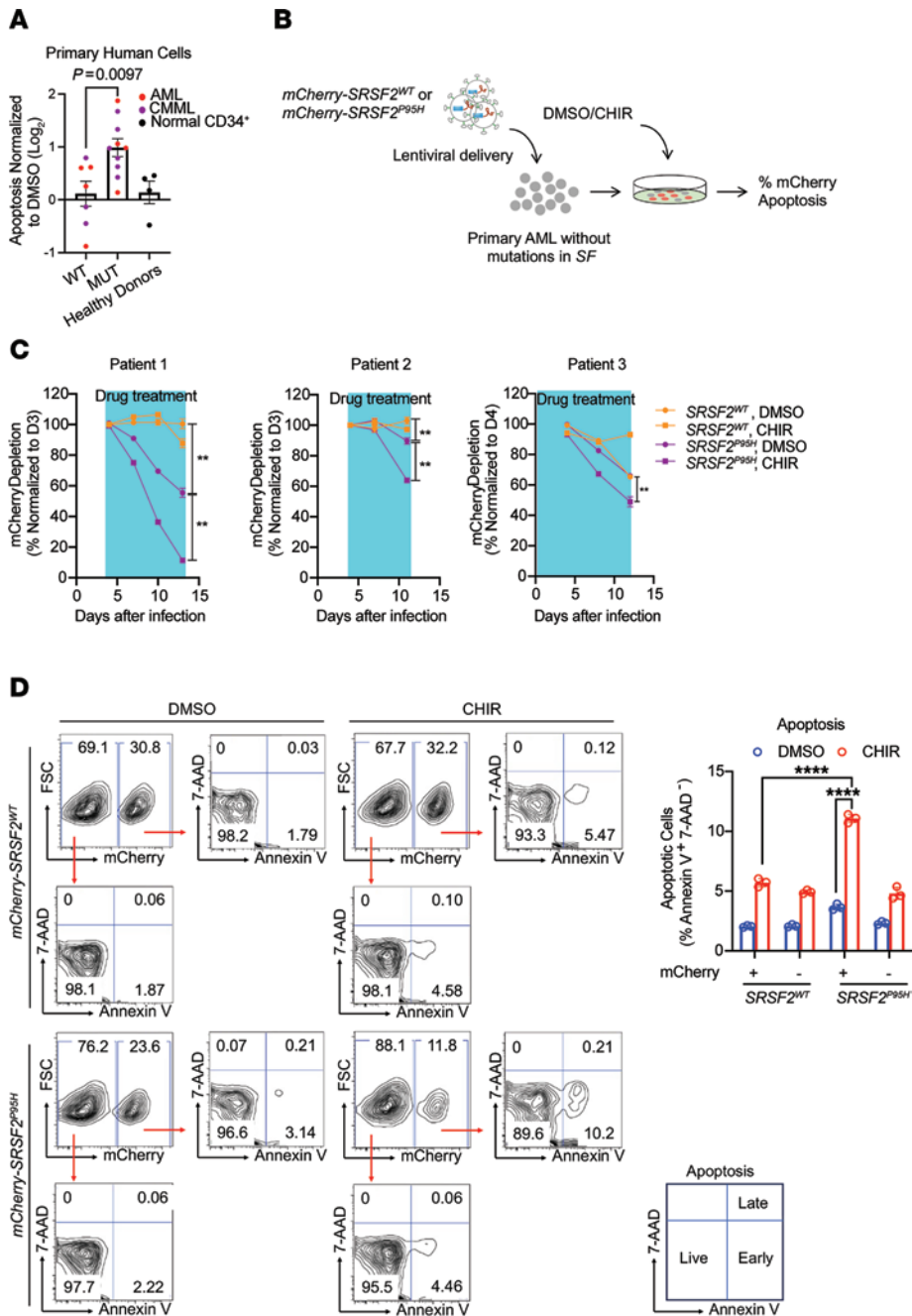


Figure 2. Selective cytotoxicity of GSK-3i in primary human leukemia cells with splicing factor mutations. (A) CHIR induced higher levels of apoptosis in splicing factor mutant (MUT) cells from patients with CMML (purple) or AML (red) compared with patients with WT splicing factors or CD34⁺ cells from healthy donors (black). The log₂[fold change] in apoptosis in CHIR-treated relative to DMSO-treated cells is shown. Genetic information for each patient is shown in Supplemental Table 1. Statistical analysis was performed using a 2-tailed Mann-Whitney test. (B) Schematic of lentivirus infection in primary AML cells for apoptosis assay. (C) Primary AML cells from 3 patients were transduced with lentivirus encoding WT or mutant *SRSF2* as in B and cultured in the absence or presence of 3 μ M CHIR (blue boxes indicate duration of drug treatment). The percentage of mCherry-positive cells normalized to the number at day 3 (patients 1 and 2) or day 4 (patient 3) is shown. (D) Representative flow cytometric analysis (left) and quantification (right) of apoptosis in primary cells from patients with AML overexpressing either *SRSF2^{*}* or *SRSF2^{P95H}*, as measured by annexin V and 7-AAD staining in the absence or presence of 3 μ M CHIR. Data in C and D are presented as the mean \pm SD; ** $P < 0.01$ and **** $P < 0.0001$ (2-way ANOVA with Šidák's multiple-comparison test).

cells (Figure 4C). This change in *PINK1* abundance was not due to a change in transcription, as detection of primary transcripts with PCR primers that detect intron 1 or intron 5 showed no significant difference in nascent transcripts with GSK-3i in WT or splicing factor mutant cells (Figure 4D). Qualitative RT-PCR with primers that span exons 6 and 7 confirmed that GSK-3i with CHIR (Figure

4E) or AR-A014418 (Supplemental Figure 4) impaired excision of intron 6, increasing intron 6 retention (568 bp), in *SRSF2^{+/+}*, *SRSF2^{P95H/+}*, and *SF3B1^{K700E/+}* K562 cells. CHIR also promoted retention of intron 6 in primary cells from patients with AML or CMML and CD34⁺ cells from healthy donors (Figure 4F). To confirm that CHIR impairs *PINK1* splicing through inhibition of GSK-3, we

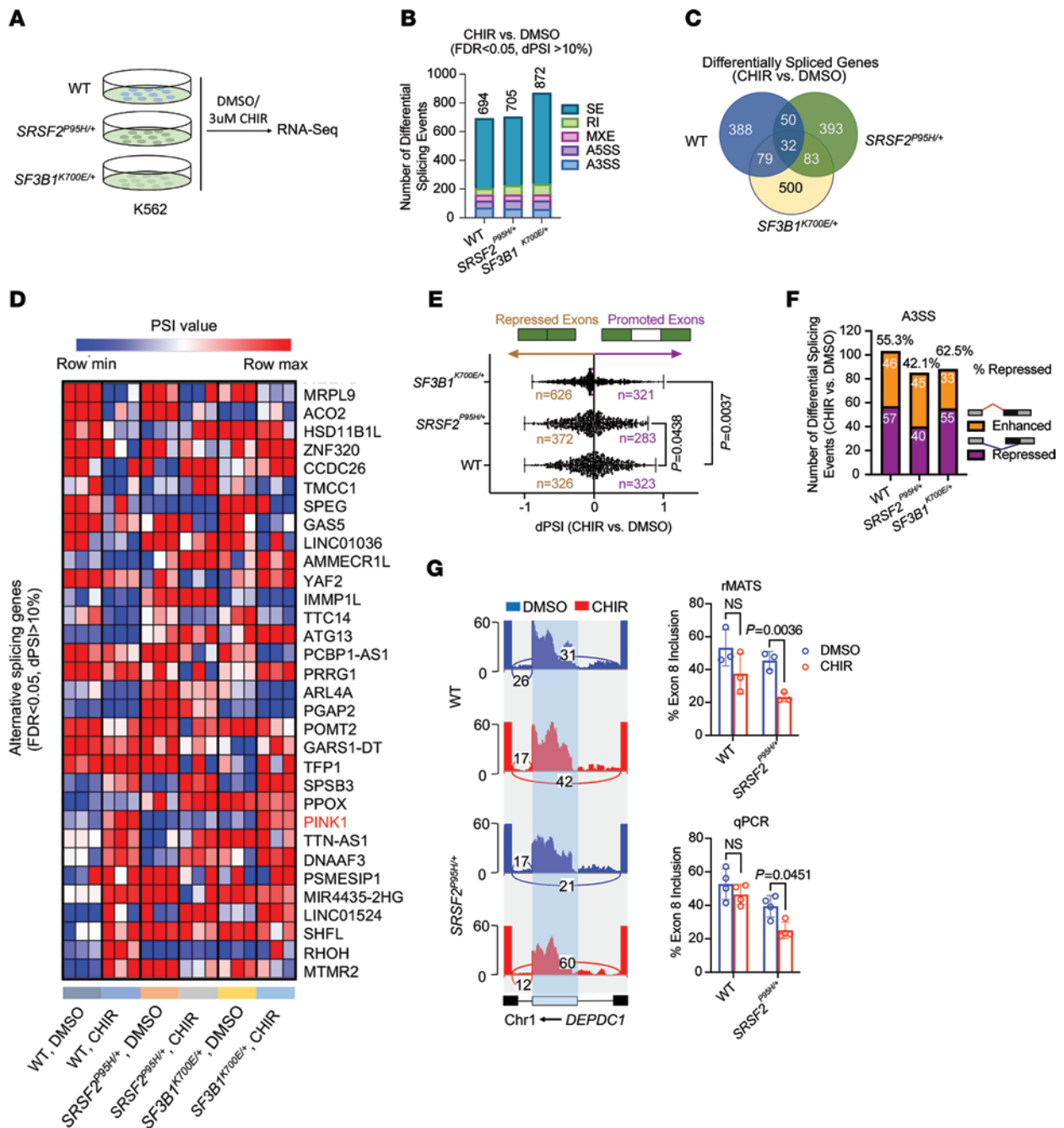


Figure 3. GSK-3i is associated with global alterations in gene expression and splicing in human leukemic cells. (A) Schematic of deep RNA-Seq in WT, *SRSF2*^{P95H/+}, and *SF3B1*^{K700E/+} K562 cells treated with DMSO or 3 μM CHIR for 24 hours. (B) Bar graphs show numbers of differential splicing events (FDR < 0.05, dPSI > 10%) in WT, *SRSF2*^{P95H/+}, and *SF3B1*^{K700E/+} K562 cells treated with CHIR versus DMSO controls. A3SS, alternative 3' splice site; A5SS, alternative 5' splice site; MXE, mutually exclusive exon; RI, retained intron; SE, skipped exon. (C) Venn diagram showing the number of overlapping alternatively spliced genes between CHIR and DMSO in WT, *SRSF2*^{P95H/+}, and *SF3B1*^{K700E/+} K562 cells. (D) Heatmap of PSI values for overlapping alternatively spliced genes comparing CHIR and DMSO in WT, *SRSF2*^{P95H/+}, and *SF3B1*^{K700E/+} K562 cells. (E) Scatterplots of cassette exon inclusion in WT, *SRSF2*^{P95H/+}, and *SF3B1*^{K700E/+} K562 cells treated with 3 μM CHIR relative to DMSO-treated controls. Numbers in brown (left) and purple (right) indicate number of cassette exons whose inclusion is repressed or promoted, respectively, in CHIR- relative to DMSO-treated cells. *P* values were determined by 1-way ANOVA with Šidák's multiple-comparison test. (F) Bar graphs show numbers of alternative 3' splice site events upon CHIR treatment compared with DMSO in WT, *SRSF2*^{P95H/+}, and *SF3B1*^{K700E/+} K562 cells. Purple and orange indicate intron-proximal 3' splice sites whose usage is repressed or enhanced, respectively, in CHIR-treated relative to DMSO-treated cells. (G) Left: Sashimi plots of *DEPDC1* in WT and *SRSF2*^{P95H/+} cells treated with DMSO or CHIR. Right: Bar plots show quantification of percentage of exon inclusion based on rMATS analysis (top) and on isoform-specific qPCR validation (bottom). Percentage of exon inclusion was quantified by RT-qPCR analysis of mRNA levels containing the cassette exons normalized to total mRNA levels. Data are presented as the mean ± SD. *P* values were determined by 2-way ANOVA with Šidák's multiple-comparison test.

tested *PINK1* splicing in WT and *GSK3A/B*-DKO cells. Similarly to CHIR and AR-AO14418, *GSK3A/B* DKO impaired intron 6 excision. In contrast, overexpression of *GSK3B* in DKO cells restored excision of intron 6 (Figure 4G). Blocking NMD by knockdown of *UPF1*, a core NMD factor, increased the mRNA stability and expression of the intron 6-retained form of *PINK1* (Figure 4H). Taken together, these data show that GSK-3 regulates *PINK1* splicing and that CHIR reduces *PINK1* mRNA abundance specifically by inhibiting GSK-3 and promoting retention of an intron containing an in-frame PTC.

SRSF2^{P95H} increases PINK1 expression and mitophagy. In contrast to GSK-3i, the *SRSF2^{P95H}* mutation markedly increased *PINK1* mRNA abundance in comparison with parental and *SF3B1^{K700E/+}* cells (Figure 4C). Nascent *PINK1* transcripts were not increased in *SRSF2^{P95H/+}* cells (Figure 4D), indicating that the increase in mRNA abundance was due to stabilization of the *PINK1* transcript rather than increased transcription. In support of this, excision of intron 6 was increased in *SRSF2^{P95H/+}* cells compared with parental cells or *SF3B1^{K700E/+}* cells (Figure 4E). Increased excision of intron 6 was further validated in TF-1 cells overexpressing *SRSF2^{P95H}* compared with cells expressing *SRSF2^{WT}* (Supplemental Figure 5A). *PINK1* activates mitophagy, and in parallel with the increase in *PINK1* levels, expression of other mitophagy-related genes, including *OPTN*, *ULK1*, *TOMM7*, *CALCOCO2*, *NBR1*, and *TAX1BP1*, was significantly increased in *SRSF2^{P95H/+}* cells (Figure 5A). The increase in *PINK1* and other mitophagy markers was associated with a substantial increase in mitophagy specifically in *SRSF2^{P95H/+}* cells, as determined by the colocalization of TOMM20 (mitochondrial marker) and LAMP1 (lysosomal marker) (Figure 5B). Immunofluorescent staining demonstrated that *PINK1* colocalizes with TOMM20 (Supplemental Figure 5B) and PARKIN (Supplemental Figure 5C), suggesting that *PINK1* was stabilized on impaired mitochondria in *SRSF2^{P95H/+}* cells. Transmission electron microscopy (TEM) showed accumulation of autophagic vacuoles with defective mitochondria with swollen matrix and collapsed cristae enclosed by a double membrane in *SRSF2^{P95H/+}* cells (Figure 5C). As *SRSF2^{P95H}* and GSK-3i appear to have opposing effects on *PINK1* splicing and abundance, we tested the effect of CHIR on mitophagy in *SRSF2^{P95H/+}* cells and found that GSK-3i impaired mitophagy in *SRSF2^{P95H/+}* cells (Figure 5, B and C), in parallel with the reduction in *PINK1* mRNA. We then assessed mitophagic flux by evaluating the accumulation of mitochondria with MitoTracker Green (MTG) staining in the presence of chloroquine (CQ), which blocks the final step of autophagy/mitophagy, fusion with the lysosome, by inhibiting lysosomal acidification. CQ increased mitochondrial mass, as expected (Supplemental Figure 5D). The increase was significantly higher in *SRSF2^{P95H/+}* cells than in *SRSF2^{+/+}* cells. Mitophagic flux was then determined by subtraction of the MTG value for untreated cells from the value for cells treated with CQ (31). The *SRSF2^{P95H/+}* mutation significantly enhanced mitophagic flux (Figure 5D). A similar increase in mitophagic flux was observed with Lys05, an alternative inhibitor of lysosomal acidification (Figure 5D). GSK-3i also increased mitochondrial mass in both *SRSF2^{+/+}* and *SRSF2^{P95H/+}* cells, with or without CQ or Lys05 (Supplemental Figure 5, D and E), consistent with reduced *PINK1* levels and impaired mitophagy. Western blot analysis confirmed that *PINK1* protein was increased in *SRSF2^{P95H/+}* cells and decreased upon CHIR treatment (Figure 5E).

To address whether an increase in mitophagy is a feature of primary cells from patients with hematologic malignancies, we queried The Cancer Genome Atlas (TCGA) database for expression of markers of mitophagy in hematologic malignancies with or without the *SRSF2* mutation. Expression of the canonical mitophagy markers *OPTN* ($P = 0.0015$) and *TOMM7* ($P = 0.0004$) was significantly increased in patients with *SRSF2^{P95*}* ($n = 43$) compared with patients with WT *SRSF2* ($n = 538$) (Figure 5F). No significant difference was observed between patients with WT and mutant *SF3B1* (Supplemental Figure 5F). These data show elevated mitophagy marker expression specifically in *SRSF2*-mutant MDS and AML, and we therefore focused on the impact of *SRSF2^{P95H}* on mitochondrial function and the role of GSK-3-dependent *PINK1* splicing in the regulation of mitophagy in *SRSF2^{P95H/+}* cells.

The SRSF2 mutation is associated with accumulation of defective mitochondria. This increase in mitophagy indicates that the *SRSF2^{P95H/+}* mutation causes mitochondrial dysfunction, which could arise through mis-splicing of nuclear mRNAs encoding mitochondrial proteins. We analyzed splicing variations in *SRSF2^{P95H/+}* cells compared with *SRSF2^{+/+}* cells (Supplemental Figure 6A). Gene Ontology (GO) analysis of differentially spliced genes in *SRSF2^{P95H/+}* cells revealed enrichment of processes related to regulation of protein targeting to mitochondrion organization, mitochondrial genome maintenance, mitochondrial respiratory chain complex I assembly, and oxidative phosphorylation (Figure 6A and Supplemental Table 4). We identified 12 alternatively spliced mRNAs that are associated with mitochondrial respiratory chain complex I (Figure 6A and Supplemental Figure 6B). These findings are consistent with GO analyses in *SRSF2*-mutant cells from primary MDS (9), CMML (Figure 6B) (7), and AML patients (Figure 6B) (7, 32), which similarly showed enrichment of mitochondrial genes in the set of alternatively spliced mRNAs.

To further assess the consequences of *SRSF2* mutation for the cellular proteome in myeloid neoplasms, we performed quantitative mass spectrometry (qMS) with a focus on the mitochondrial proteome by using human proteome (UniProtKB) and mitochondrial (MitoCarta3.0) databases for protein identification (Figure 6C). We identified 163 mitochondrial proteins whose levels are affected by *SRSF2* mutation (Supplemental Table 5). The 84 proteins that showed significantly reduced levels in *SRSF2^{P95H/+}* cells included multiple mitochondrial ribosomal proteins (Figure 6D). Of the 6 respiratory mitochondrial complex I proteins detected by qMS, 5 were significantly downregulated by *SRSF2* mutation (Figure 6D).

Evaluation of the mitochondrial properties of *SRSF2^{P95H/+}* cells revealed elevated mitochondrial mass in comparison with *SRSF2^{+/+}* cells based on MTG staining (Figure 6E) and immunostaining of the outer membrane protein TOMM20 (Supplemental Figure 6C). In contrast, mitochondrial mass was not increased in *SF3B1^{K700E/+}* cells (Supplemental Figure 6D). Overexpression of *SRSF2^{P95H}* also increased mitochondrial content in K562, TF-1, and primary AML cells when compared with overexpression of WT *SRSF2* (Supplemental Figure 6, E–G). Mitochondrial DNA (mtDNA) copy number, which correlates with mitochondrial biogenesis, significantly increased (Figure 6F), suggesting that elevated mitophagy in *SRSF2^{P95H}* cells is balanced by increased mitochondrial biogenesis. This dynamic ultimately leads to increased mitochondrial content.

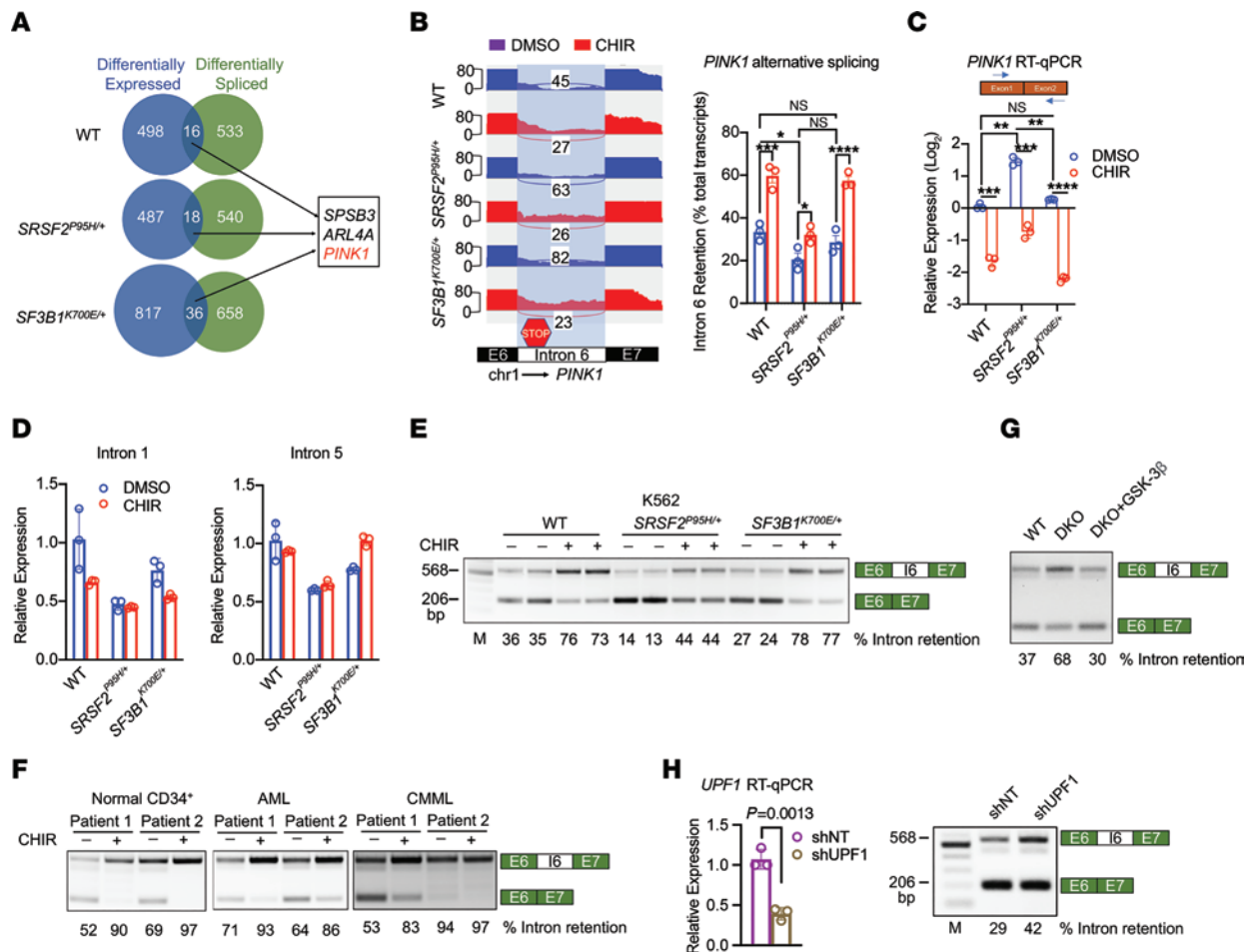


Figure 4. GSK-3 regulates *PINK1* splicing. (A) Venn diagram of genes differentially expressed (blue) or differentially spliced (green) in CHIR-treated WT, *SRSF2*^{P95H/+}, and *SF3B1*^{K700E/+} K562 cells relative to DMSO-treated controls. (B) Left: Sashimi plots of *PINK1* in WT, *SRSF2*^{P95H/+}, and *SF3B1*^{K700E/+} cells treated with DMSO or CHIR. Right: Bar graph shows intron 6 retention as a percentage of total transcripts. (C) *PINK1* mRNA levels in WT, *SRSF2*^{P95H/+}, and *SF3B1*^{K700E/+} cells treated with DMSO or 3 μM CHIR for 24 hours detected by RT-qPCR using primers that span exons 1 and 2 (mean ± SD). For data in B and C, **P* < 0.05, ***P* < 0.01, ****P* < 0.001, and *****P* < 0.0001 (2-way ANOVA with Šidák's multiple-comparison test). (D) *PINK1* nascent transcript detection by RT-qPCR using primers for intron 1 (left) and intron 5 (right) in WT, *SRSF2*^{P95H/+}, and *SF3B1*^{K700E/+} cells treated with DMSO or 3 μM CHIR for 24 hours. (E and F) Representative RT-PCR with primers spanning exon 6 (E6), intron 6 (I6), and exon 7 (E7) of *PINK1* in WT, *SRSF2*^{P95H/+}, and *SF3B1*^{K700E/+} K562 cells (E) and in CD34⁺ cells from healthy donors, primary AML cells, and CD34⁺ cells from CMML patients (F) treated with DMSO or 3 μM CHIR for 24 hours. PCR product with retained intron 6 is 568 bp, and product for spliced exon 6-7 (without retained intron) is 206 bp. M, DNA marker. (G) RT-PCR analysis of *PINK1* splicing in WT, *GSK3A/B*-DKO, and *GSK3A/B*-DKO cells overexpressing GSK-3β (HEK293T). (H) *UPF1* mRNA levels detected in K562 cells transduced with lentivirus expressing shRNA against *UPF1* compared with non-targeting control (left), and levels of intron-retained and -spliced *PINK1* mRNAs following *UPF1* knock-down compared with control measured by RT-PCR (right). Data are presented as the mean ± SD. *P* value was determined by 2-tailed Student's *t* test.

Mitochondrial membrane potential (MMP) per unit mitochondrial mass as assessed by tetramethylrhodamine ethyl ester (TMRE)/MTG ratio and mitochondrial reactive oxygen species (mtROS) levels were significantly higher in *SRSF2*^{P95H/+} cells (Figure 6, G and H). This chronic oxidative stress may damage the mitochondria and mtDNA. To test mitochondrial function, we subjected parental and *SRSF2*^{P95H/+} cells to high-resolution respirometry. Surprisingly, both the basal and the maximal respiratory capacity were significantly lower in *SRSF2*^{P95H/+} cells (Figure 6I). As *SRSF2* mutation dramatically altered the splicing of complex I-related genes and reduced complex I protein levels, we further tested complex I respiratory capacity. Complex I-linked respiration, which was measured by sequential addition of the complex I-linked substrates pyruvate, malate, and glutamate (P/M/G) and ADP, was also significantly lower in *SRSF2*^{P95H/+} cells relative to *SRSF2*^{+/+} cells (Figure 6I). The elevated mitochondrial

mass and MMP in *SRSF2*^{P95H/+} cells therefore could not maintain high respiratory capacity. These functional data together with the increase in mitophagy demonstrate a marked defect in mitochondrial function associated with the leukemogenic *SRSF2*^{P95H} mutation.

We next treated WT and *SRSF2*^{P95H/+} K562 cells with a mitochondrial uncoupler, carbonyl cyanide *m*-chlorophenylhydrazone (CCCP), and then measured mitochondrial depolarization occurring during apoptosis using JC-1 staining (33). Although WT cells responded to CCCP treatment with reduced MMP, the *SRSF2* mutation further decreased MMP, suggesting a higher demand for efficient mitophagy in response to mitochondrial stress in *SRSF2*^{P95H/+} cells (Figure 6J). Overall, these data support a model in which splicing defects associated with the *SRSF2* mutation disrupt mitochondrial function and lead to compensatory increased mitochondrial content and turnover.

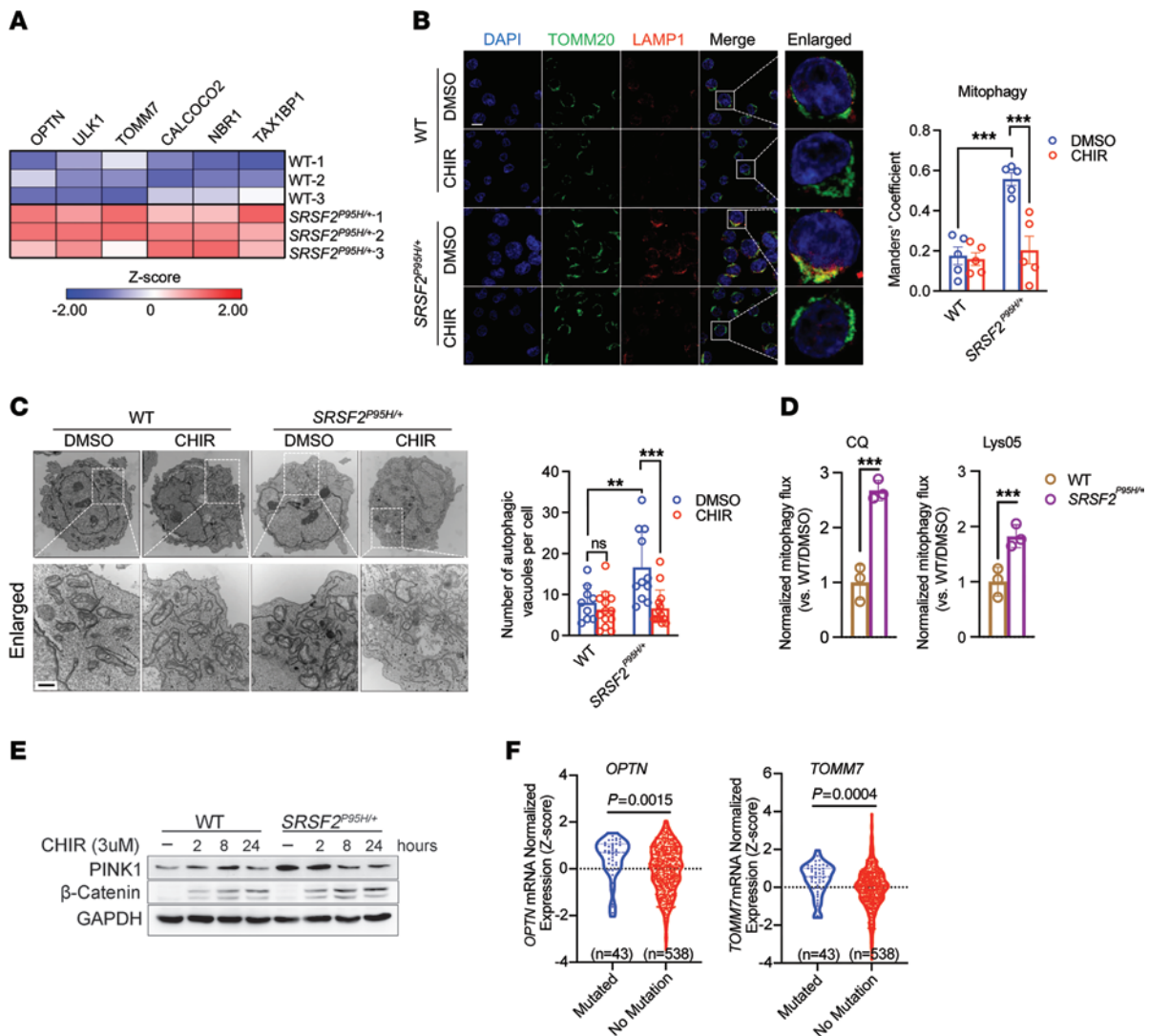


Figure 5. *SRSF2*^{P95H} increases *PINK1* expression and mitophagy. (A) Heatmap shows z-scored expression of mitophagy-related genes in WT and *SRSF2*^{P95H/+} K562 cells. (B) Left: Representative confocal images of mitochondria (green, TOMM20⁺) and lysosomes (red, LAMP1⁺) in K562 WT or *SRSF2*^{P95H/+} cells treated with DMSO or 3 μ M CHIR for 2 days. Scale bar: 10 μ m. Right: Bar plot shows quantification of the colocalization of mitochondria with lysosomes ($n = 5$ fields for each group; $n = 3$). (C) Left: Representative transmission electron microscopy images of WT and *SRSF2*^{P95H/+} K562 cells treated with DMSO or 3 μ M CHIR for 2 days. Scale bar: 0.5 μ m. Right: Bar plot shows quantification of the number of autophagic vacuoles per cell. Each circle represents one cell. (D) Bar graph shows mitophagic flux determined by MitoTracker green (MTG) staining in WT and *SRSF2*^{P95H/+} K562 treated with or without 2 μ M CHIR for 48 hours. Mitochondrial net flux was calculated by mitochondrial accumulation in the presence of 100 μ M chloroquine (CQ) or 50 μ M Lys05 for 4 hours (31). Data are presented as the mean \pm SD. For data in B–D, ** $P < 0.01$ and *** $P < 0.001$ (2-way ANOVA with Sidák's multiple-comparison test). (E) Immunoblotting of *PINK1* and β -catenin in WT and *SRSF2*^{P95H/+} cells treated with DMSO or 3 μ M CHIR for indicated times. (F) Violin plot of *OPTN* and *TOMM7* normalized expression in AML patients in TCGA data set ($n = 581$) with or without mutations in *SRSF2*. Statistical analysis was performed using 2-tailed Mann-Whitney test.

As *SRSF2*^{P95H} increases the abundance of *PINK1* mRNA, we further hypothesized that mitochondrial dysfunction signals to the splicing apparatus to promote excision of intron 6, stabilizing *PINK1* mRNA to meet an increased demand for mitophagy. In support of this hypothesis, addition of CCCP promoted excision of intron 6 in a dose-dependent manner in cells with WT *SRSF2* and to an even greater extent in *SRSF2*^{P95H/+} cells (Figure 6K). Consistent with the destabilizing impact of the PTC in intron 6, this shift in splicing was associated with an increase in *PINK1* mRNA abundance (Figure 6L). This response in cells with WT *SRSF2* suggests a general mechanism, independent of the *SRSF2* mutation, for

sensing mitochondrial stress through modulation of *PINK1* splicing, leading to increased expression of *PINK1* mRNA and protein.

Increased mitophagy is a therapeutic vulnerability in SRSF2-mutant hematologic malignancies. GSK-3i reduces *PINK1* expression, impairs mitophagy, and is selectively lethal to *SRSF2*^{P95H/+} cells. Given that *PINK1*-mediated mitophagy is required for the survival of normal hematopoietic stem cells (HSCs) (34) and acute myeloid leukemia stem cells (35, 36), we hypothesized that a greater dependency on *PINK1*-mediated mitophagy upon stress may be the basis for the selective toxicity of GSK-3i to *SRSF2*^{P95H/+} cells. To explore this hypothesis, we evaluated the effects of GSK-3i on

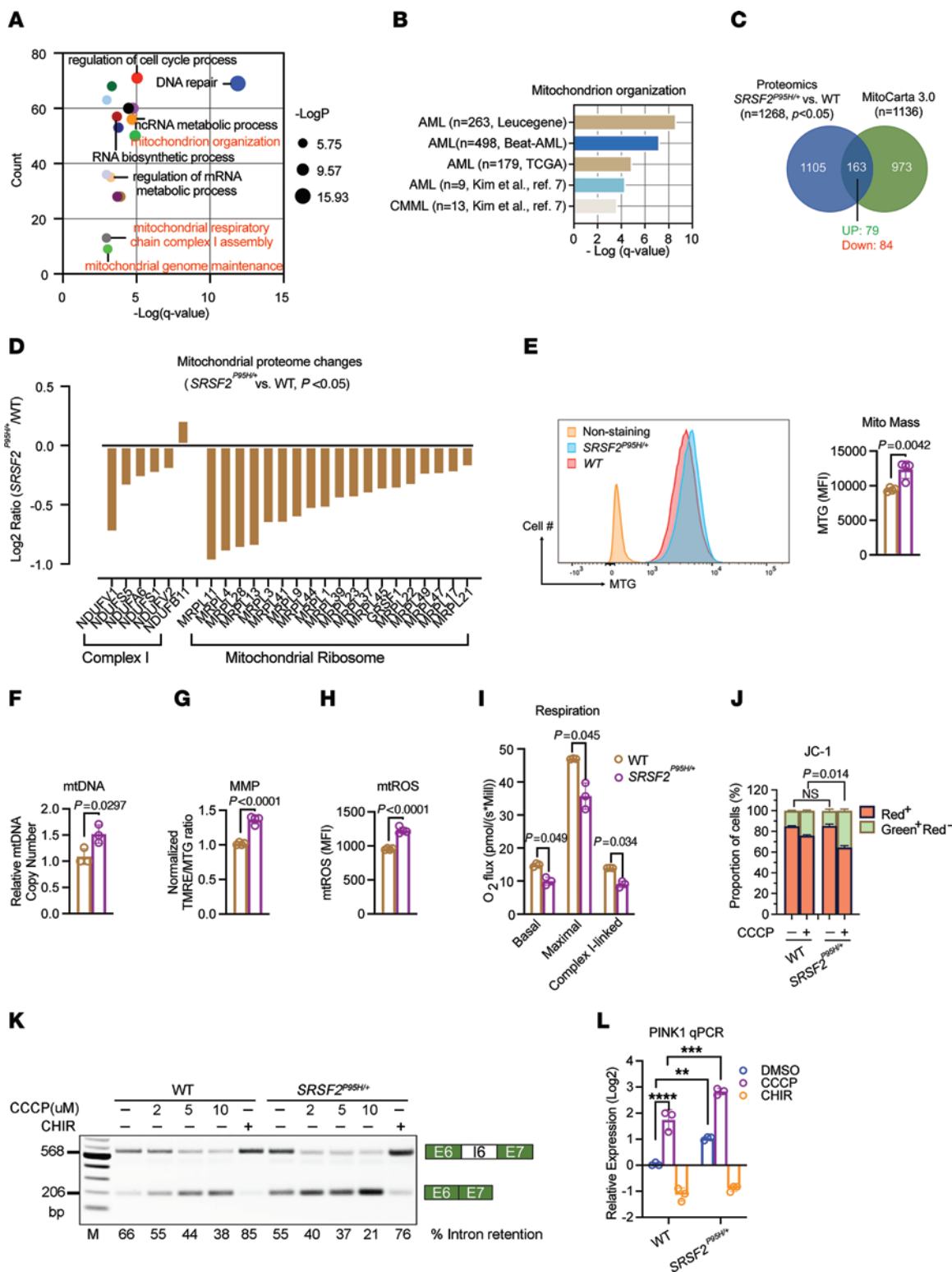


Figure 6. The *SRSF2* mutation is associated with accumulation of defective mitochondria. (A) Bubble plot for GO enrichment analysis of differentially spliced genes in *SRSF2*-mutant versus WT K562 cells. The y axis shows the number of genes; the x axis denotes $-\log[q]$ value. The size of each circle represents $-\log[P]$ value. (B) Bar graph for GO enrichment analysis of differentially spliced genes in *SRSF2*-mutant cells versus *SRSF2*^{+/+} primary CMML and AML patient samples shows significantly dysregulated pathway associated with mitochondrion organization, with Fisher's exact test $-\log[q]$ value on x axis. (C) Venn diagram showing overlap of proteins differentially expressed in *SRSF2*^{P95H/+} versus WT K562 cells and MitoCarta3.0 database. (D) Bar graph shows log₂ ratio of selected mitochondrial protein in *SRSF2*^{P95H/+} versus *SRSF2*^{+/+} K562 cells. (E–H) Quantification of mitochondrial parameters in WT and *SRSF2*^{P95H/+} cells (mean ± SD). (E) MTG. (F) Mitochondrial DNA copy number. Data are shown as ratio of mitochondrial DNA (mt-ND1) to nuclear DNA (B2M) in WT and *SRSF2*^{P95H/+} cells. (G) MMP per mitochondrion. (H) Mitochondrial ROS (mtROS). (I) Basal, maximal, and complex I-linked mitochondrial respiratory capacity was measured in WT and *SRSF2*^{P95H/+} cells. Maximal respiratory capacity was measured after FCCP injection. Complex I-linked respiration was measured by sequential addition of the complex I-linked substrates pyruvate, malate, and glutamate (P/M/G) and ADP. Oxygen flux is expressed as respiration per million cells [pmol/(s·10⁶ cells)], mean ± SD of $n = 3$ independent cultures. Each sample was measured in duplicate. P values were determined by 2-tailed Student's t test (E–I). (J) Analysis of mitochondrial depolarization in WT and *SRSF2*^{P95H/+} cells treated with DMSO or 2 μM CCCP for 24 hours using JC-1 staining, in which a high red⁺/green⁺ ratio indicates high MMP ($n = 3$). Statistical analysis was by 2-tailed χ^2 test. (K) Representative RT-PCR results of *PINK1* splicing in WT and *SRSF2*^{P95H/+} cells treated with DMSO, 3 μM CHIR, or indicated concentrations of CCCP for 24 hours. (L) RT-qPCR analysis of *PINK1* mRNA levels in WT and *SRSF2*^{P95H/+} cells treated with DMSO, 3 μM CHIR, or 2 μM CCCP for 24 hours (mean ± SD). ** $P < 0.01$, *** $P < 0.001$, and **** $P < 0.0001$ (2-way ANOVA with Šidák's multiple-comparison test).

mitochondria. GSK-3i increased MMP (Figure 7A) and promoted accumulation of mitochondrial mass in K562 cells with WT *SRSF2* (Figure 7B and Supplemental Figure 7A), consistent with previous reports in mouse cardiomyocytes and HSCs (37, 38). GSK-3i in *SRSF2*^{P95H/+} cells impaired mitophagy (Figure 5, B and C) and further increased MMP (Figure 7A) and mitochondrial content (Figure 7B and Supplemental Figure 7, A–D) in comparison with WT counterparts. Gene set enrichment analysis (GSEA) revealed that GSK-3i with CHIR strongly enriched for genes representing enhanced mitochondrial biogenesis and oxidative phosphorylation, a mitochondrial stress that may increase the requirement for *PINK1*-mediated mitochondrial surveillance (Figure 7C).

To test directly whether GSK-3i-induced alternative splicing of *PINK1* causes cell death in *SRSF2*^{P95H/+} cells, we expressed a *PINK1* cDNA lacking intron 6 and treated with CHIR (Figure 7D). Expression of full-length *PINK1* completely rescued the cell death caused by GSK-3i in *SRSF2*^{P95H/+} cells (Figure 7E), demonstrating an essential role for *PINK1* mis-splicing in the preferential cytotoxicity of GSK-3i in *SRSF2*-mutant cells.

Our data indicate that increased mitophagy is a targetable vulnerability in *SRSF2*^{P95H/+} cells. We tested this hypothesis further by inhibiting mitophagy downstream of *PINK1* by treating *SRSF2*^{+/+} and *SRSF2*^{P95H/+} cells with the lysosomal inhibitor CQ. Inhibiting mitophagy with CQ caused accumulation of mitochondria (Figure 7F) and preferentially killed *SRSF2*^{P95H/+} cells (IC₅₀ = 14.1 μM) compared with *SRSF2*^{+/+} cells (IC₅₀ = 29.1 μM) (Figure 7G and Supplemental Figure 7E). Preferential sensitivity of *SRSF2*^{P95H/+} cells to autophagy inhibitors was further validated with LysO5 (39, 40),

a potent dimeric form of CQ (Figure 7H and Supplemental Figure 7F). Next, we introduced *SRSF2*^{P95H} or *SRSF2*^{WT} into *SRSF2*^{+/+} primary AML cells along with the mCherry reporter (Figure 7I and Supplemental Table 1). Expression of *SRSF2*^{P95H} resulted in increased sensitivity to CQ (Figure 7J) and LysO5 (Figure 7K) in comparison with primary AML cells expressing *SRSF2*^{WT}.

Together, these data support the hypothesis that aberrant splicing of *PINK1* caused by GSK-3i reduces *PINK1* expression and inhibits clearance of defective mitochondria in *SRSF2* mutant cells, disrupting the homeostatic balance required for survival. Targeting mitophagy therefore represents a promising therapeutic strategy to eradicate *SRSF2*-mutant hematologic malignancies (Figure 8).

Discussion

Splicing factor mutations are common in MDS and AML (2, 41, 42), but how these mutations alter cellular function remains unclear. The results presented here show a marked increase in mitophagy specifically in *SRSF2*-mutant MDS and AML compared with other forms of AML and MDS. The recurrent *SRSF2*^{P95H} mutation alters the splicing of mRNAs encoding mitochondrial proteins, disrupts mitochondrial function, and increases mitochondrial mass and turnover, reflecting a dependency on a higher level of mitophagy for survival. Our results identify a mechanism of mitochondrial surveillance in which mitochondrial dysfunction enhances the splicing of *PINK1* mRNA to a more stable form, leading to increased abundance of *PINK1* mRNA and protein. Inhibition of GSK-3 impairs *PINK1* splicing, reduces mitophagy, and selectively kills cells with the *SRSF2*^{P95H} mutation. Inhibition of mitophagy by targeting of lysosomal function is also lethal to *SRSF2*^{P95H/+} cells. These data therefore reveal a dependency of splicing factor mutant MDS and AML and identify potential therapeutic targets for these hematologic malignancies.

The altered splicing of nuclear-encoded mitochondrial mRNAs observed here fits well with previous work identifying altered splicing of mRNAs involved in mitochondrial function in primary cells from MDS and AML patients with the *SRSF2*^{P95} mutation (7, 9, 32). We also find that markers of mitophagy are robustly increased in AML and MDS patients with the *SRSF2*^{P95/+} mutation in the TCGA data set. Mitochondrial turnover is required for self-renewal of normal HSCs (34, 43, 44) and leukemic stem cells (36, 44, 45), and was recently shown to mediate resistance to BH3 mimetics in AML cells (46–49). Thus, while inhibition of mitophagy or autophagy has been shown to be toxic to AML cells (36, 40, 45, 46), a mechanism for increased mitophagy in AML has not previously been defined. Our data demonstrate significantly greater sensitivity to mitophagy/autophagy inhibitors in *SRSF2*^{P95/+} cells, reveal a mechanism connecting this leukemogenic splicing factor mutation to mitochondrial dysfunction and increased mitophagy, and identify *PINK1* splicing as a targetable vulnerability in *SRSF2*-mutated AML and MDS.

The data presented here reveal a homeostatic mechanism for the regulation of mitochondrial clearance. Prior work has established that, under basal conditions, *PINK1* protein is degraded within mitochondria with a high MMP, whereas low MMP associated with mitochondrial dysfunction allows *PINK1* protein stabilization and initiation of mitophagy (50). The homeostatic mechanism described here functions by altering *PINK1*

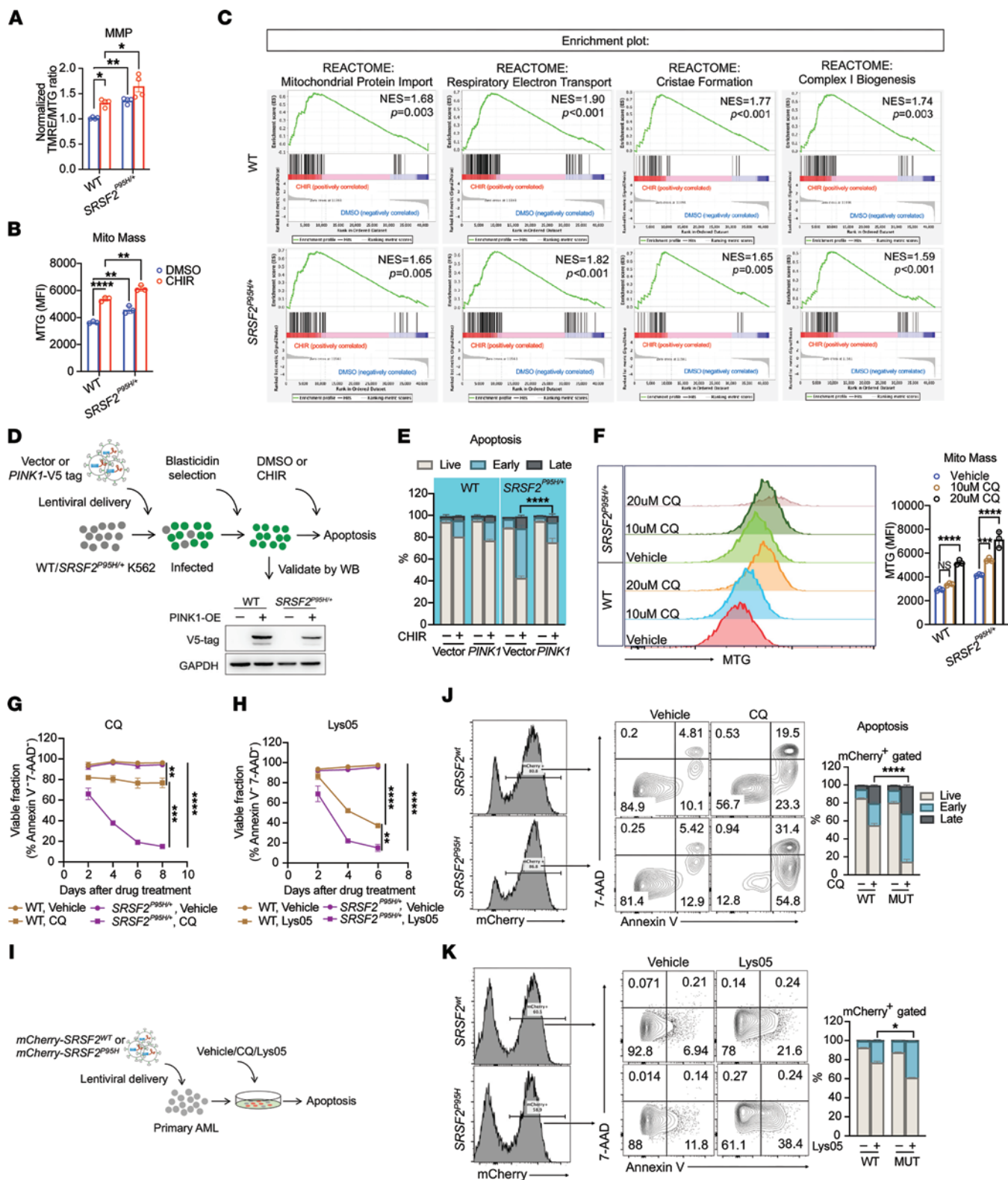


Figure 7. Targeting mitophagy in *SRSF2*-mutant hematologic malignancies. (A and B) Quantification of mitochondrial parameters in WT and *SRSF2*^{P95H/+} cells treated with DMSO or 3 μM CHIR. (A) MMP per mitochondrion. (B) MTG. (C) GSEA showing mitochondria-related enrichment plots for CHIR- versus DMSO-treated WT and *SRSF2*^{P95H/+} cells. (D) Schematic of generation of WT and *SRSF2*^{P95H/+} stable lines overexpressing *PINK1* for apoptosis assay with or without CHIR. (E) Percentages of viable and early- and late-apoptotic cells in *PINK1*-overexpressing WT and *SRSF2*^{P95H/+} cells treated with DMSO or 3 μM CHIR in vitro for 8 days. (F) Quantification of mitochondrial mass by MTG staining in WT and *SRSF2*^{P95H/+} cells treated with vehicle or indicated concentrations of CQ for 6 days. (G and H) Percentage of viable cells based on 7-AAD and annexin V flow cytometric analysis of WT and *SRSF2*^{P95H/+} cells treated with vehicle, 20 μM CQ (G), or 2 μM Lys05 (H) in vitro. (I) Schematic representation of lentiviral delivery of *SRSF2*^{WT} or *SRSF2*^{P95H} to primary AML cells for CQ and Lys05 treatment followed by apoptosis assay. (J and K) Representative flow cytometric analysis (left) and quantification (right) of apoptosis in primary cells from patients with AML overexpressing either WT or *SRSF2*^{P95H}, as measured by annexin V and 7-AAD staining in the absence or presence of 15 μM CQ (J) or 2 μM Lys05 (K) for 4 days. Data in A, B, and F–H are presented as the mean ± SD. **P* < 0.05, ***P* < 0.01, ****P* < 0.001, and *****P* < 0.0001 (2-way ANOVA with Šidák's multiple-comparison test). For data in E, J, and K, statistical analysis was performed using a 2-tailed χ^2 test.

splicing: mitochondrial dysfunction, whether caused by direct pharmacologic disruption of the MMP or indirectly by the *SRSF2* mutation, promotes the excision of a poison intron to yield a more stable *PINK1* mRNA. Although the *SRSF2*^{P95H} mutation could directly alter the splicing of *PINK1* mRNA, we propose that the mechanism is indirect. *SRSF2* typically regulates cassette exon selection, whereas we observe enhanced intron excision, and, importantly, CCCP alters *PINK1* splicing in cells with WT *SRSF2*, supporting a homeostatic mechanism that is sensitive to but independent of the *SRSF2* mutation. Although the altered splicing of *PINK1* mRNA described here is distinct from the well-established regulation of *PINK1* protein stability by MMP, both mechanisms result in increased *PINK1* protein abundance under conditions of mitochondrial stress. Our data thus support a mechanism for sensing mitochondrial stress through modulation of *PINK1* splicing, increasing *PINK1* expression to support an increased demand for mitophagy in the setting of mitochondrial dysfunction.

Splicing out of the poison intron requires GSK-3, which phosphorylates multiple core splicing factors, including *SRSF2*, and regulates splicing at a transcriptome-wide level in diverse cell types (22–26). Thus, pharmacologic inhibition or *GSK3* knockout impairs splicing of *PINK1*, leading to retention of the poison intron and reduction in overall levels of *PINK1* mRNA and protein. Altered splicing of *PINK1* explains the lethality of GSK-3 inhibitors in *SRSF2*^{P95H/+} cells, as survival in the presence of a GSK-3 inhibitor is rescued by expression of *PINK1* cDNA. Furthermore, chloroquine and Lys05, which target autophagy downstream of *PINK1*, also preferentially kill *SRSF2*^{P95H/+} cells, supporting the hypothesis that these splicing factor mutant cells are dependent on mitophagy for survival and suggesting an actionable therapeutic target in splicing factor mutant myeloid neoplasms.

Currently there are no FDA-approved drugs targeting splicing factor mutant malignancies. Here we identify mitophagy as a therapeutic vulnerability specifically in AML and MDS driven by hotspot mutations in the splicing factor *SRSF2*. We have also

uncovered a mechanism for mitochondrial surveillance that is mediated through GSK-3-dependent alternative splicing of *PINK1* and show significantly increased sensitivity to GSK-3 or autophagy inhibition in splicing factor mutant cells. Several GSK-3 inhibitors are either in wide clinical use or have been shown to be safe in phase I–III clinical trials (51–54) and could be repurposed to treat MDS. Hence targeting mitophagy with GSK-3 inhibitors or general autophagy inhibitors may provide a new opportunity to treat *SRSF2*-mutant MDS and AML.

Methods

Sex as a biological variable. This study used deidentified primary patient cells from male and female patients. However, sex was not considered as a biological variable because the study was not powered to distinguish sex differences. Xenografts of human cells into murine hosts were performed using female mice only. Sex of the host was not considered as a biological variable in these xenograft experiments.

Cell lines, primary human samples, constructs, and nucleofection. Bone marrow- or peripheral blood-derived mononuclear cells (MNCs) from AML or CMML patients were obtained from the Stem Cell and Xenograft Core Facility at the University of Pennsylvania (RRID: SCR_010035). Detailed patient characteristics are listed in Supplemental Table 1. CD34⁺ cells were purified from CMML patients through immunomagnetic selection (Miltenyi Biotec) according to the manufacturer's instructions. CD34⁺ cells from healthy donors were purchased from STEMCELL Technologies. Cryopreserved AML MNCs were resuspended in IMDM supplemented with 15% BIT (BSA, insulin, transferrin; STEMCELL Technologies), 100 ng/mL SCF, 50 ng/mL FLT3L, 20 ng/mL IL-3, and 20 ng/mL G-CSF. CD34⁺ cells enriched from CMML patients or healthy donors were cultured in StemSpan SFEM II medium (STEMCELL Technologies) supplemented with 10% FBS, 1% L-glutamine, 10 ng/mL IL-3, 10 ng/mL IL-6, and 25 ng/mL SCF. TF-1 cells were maintained in RPMI supplemented with 10% FBS and 2 ng/mL hGC-SCF (PeproTech). K562 cells were cultured in IMDM supplemented with 10% FBS. Cells were maintained at 37°C and 5% CO₂. *PINK1* (pLenti6-DEST *PINK1*-V5 WT, 13320), *shUPF1* (PLKO.1-UPF1-CDS, 136037), WT (pRRL-*SRSF2*_WT_mCherry, 84020), and *P95H SRSF2* (pRRL-*SRSF2*_P95H_mCherry, 84023) lentiviral overexpression constructs were purchased from Addgene. Lentiviruses were produced and used to transduce TF-1, K562, and primary AML cells, as described previously (55). Primary AML cells (2 × 10⁶ cells) were transduced with WT and *P95H SRSF2* lentivirus by spin infection in growth medium containing 4% LentiBlast (OZ Biosciences). Transduction efficiency was 30%–60%. HEK293T cells were cultured in DMEM supplemented with 10% FBS and 1% penicillin/streptomycin. *GSK3A/B*-DKO HEK293T cells were generated by lentiviral delivery of Cas9 and guide RNA sequence targeting *GSK-3A* (GCCTAGAGT-GGCTACGACTG) and *GSK-3B* (AGATGAGGTCTATCTTAATC) followed by single clone selection as previously described (51). *GSK3A/B*-DKO HEK293T cells were transfected using Lipofectamine 3000 (Invitrogen) according to the manufacturer's instructions.

Flow cytometry, apoptosis assay, and cell cycle analysis. For flow cytometric apoptosis assay, K562, TF-1, primary AML blast, or CD34⁺ cells purified from CMML patients or healthy donors were suspended in Annexin V Binding buffer (BioLegend 422201) and incubated with anti-annexin V antibody (BioLegend 640920) and

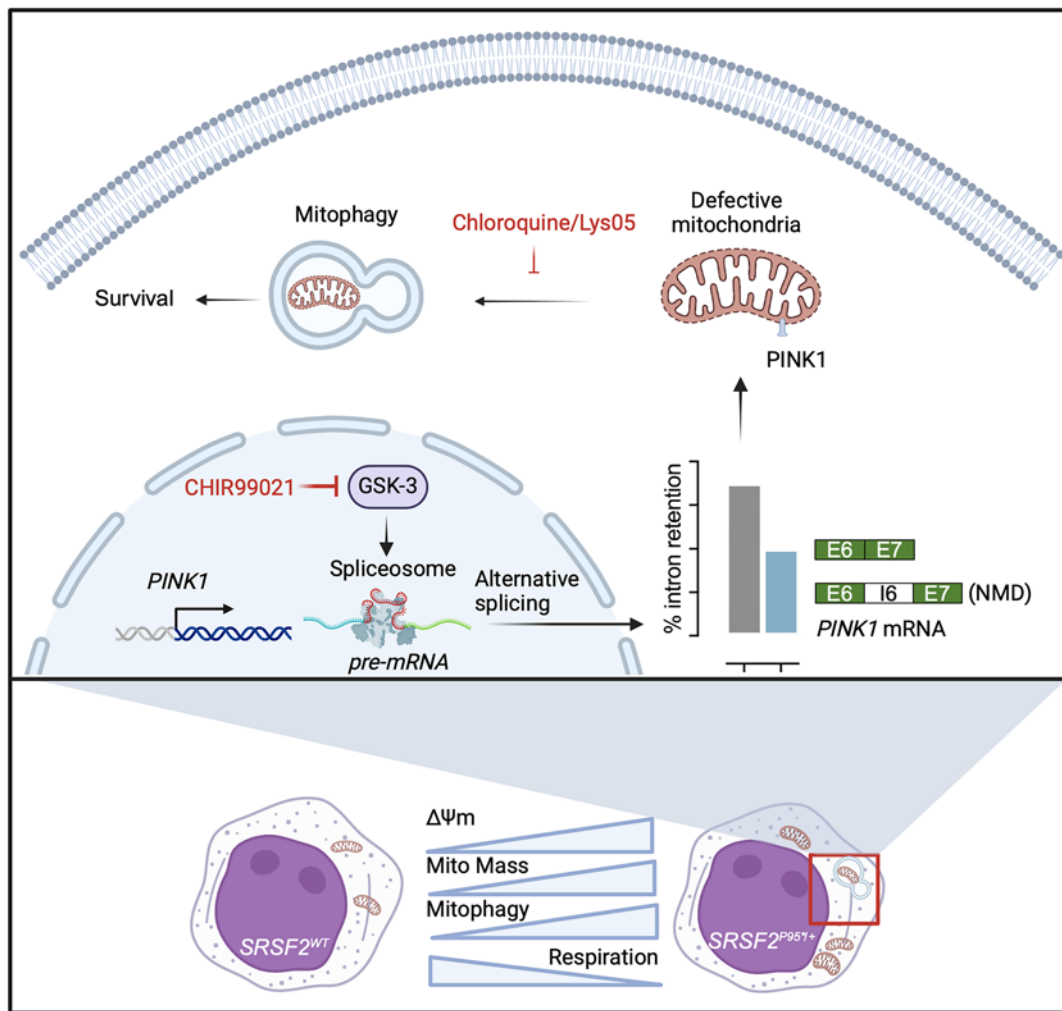


Figure 8. Proposed model for dependency of *SRSF2*-mutant leukemias on PINK1-mediated mitophagy and preferential cytotoxicity of GSK-3i and mitophagy inhibitors CQ and Lys05.

7-amino-actinomycin D (7-AAD; BioLegend 420403) for 15 minutes at room temperature in the dark. Immunophenotypes of viable cells or cells in early apoptosis or late apoptosis were defined as annexin V⁻7-AAD⁻, annexin V⁺7-AAD⁻, or annexin V⁺7-AAD⁺, respectively. For cell cycle analysis, cells were fixed and permeabilized in 70% ethanol at -20°C for 1 hour, washed in cold FACS buffer, and then stained with anti-Ki67 (BD Biosciences 350506) for 30 minutes on ice. After staining, cells were washed twice in FACS buffer and resuspended in FACS buffer containing 10 μM DAPI (BioLegend 422801). Stained cells were then tested by flow cytometry. Differences in apoptosis between culture conditions were analyzed by 2-sided χ^2 test.

Cell growth assay. Triplicates of WT and *SRSF2*^{P95H/+} K562 cells were seeded at 10,000 cells per well in 96-well plates and treated with indicated concentrations of CHIR (Cayman 13122) or chloroquine (CQ; Sigma-Aldrich C6628). Four days after culture, MTS reagent (Abcam ab197010) was added to cell medium at a final concentration of 0.5 mg/mL for 3 hours at 37°C, and cell viability was measured per the manufacturer's instructions. IC₅₀ was determined with GraphPad Prism 8 using baseline correction (by normalizing to vehicle control), the asymmetric (5-parameter) equation, and least-squares fit.

Immunoblotting. Cells were lysed in RIPA buffer plus protease inhibitor cocktail (Sigma-Aldrich P8340) and phosphatase inhibitor cocktail #2 (Sigma-Aldrich P5726) and #3 (Sigma-Aldrich P0044) used 1:100 each. Supernatants were collected after centrifugation at 20,800g for 15 minutes at 4°C, adjusted to 1× Laemmli sample buffer, and subjected to SDS-PAGE and then immunoblotted as described previously (51). Antibodies for biochemical studies included anti-GAPDH (Cell Signaling Technology [CST] 2118), anti-cleaved caspase-8 (CST 9496), anti-cleaved caspase-3 (CST 9661), anti-FLAG tag (CST 14793), anti-V5 tag (CST 13202), and anti- β -catenin (CST 9562). Other antibodies included antibodies against PINK1 (Invitrogen PA5-86941) and β -actin (Sigma-Aldrich A5441).

Real-time qPCR and RT-PCR. RNA was extracted from TF-1, K562, and primary cells using an RNeasy Kit (QIAGEN) according to the manufacturer's instructions. cDNA was synthesized using SuperScript III (Life Technologies) according to the manufacturer's instructions. For detection of PINK1 mature mRNA, the following primers were used: forward, 5'-GCCTCATCGAGGAAAAACAGG-3'; reverse, 5'-GTCTCGTGC-CAACGGGTC-3'. For detection of PINK1 pre-mRNA, the following primers were used: intron 5 forward, 5'-CCTTTGCCTGGGGATTTTGC-3';

intron 5 reverse, 5'-GGGGCTAATGGCTCAGTGTT-3'; intron 1 forward, 5'-GAGGCGAGGTCCTTAAAGC-3'; intron 1 reverse, 5'-TGCGACAGGAGCTGTAATCG-3'. For detection of the PINK1 aberrant junction, the following primers were used: forward, 5'-GGTGATCGCAGATTTTGCT-3'; reverse, 5'-GCCCGAAGATTCATAGGCG-3'. The primers used for *BCL-X* isoform-specific real-time qPCR analysis were: *BCL-X* all forward, 5'-CATCAATGGCAACCCATCCTG-3'; reverse, 5'-GCAGTTCAAACCTCGTCGCCT-3'; *BCL-Xs* forward, 5'-GAGCTTTGAACAGGATACTTTTGTGG-3'; reverse, 5'-TTCCGACTGAAGAGTGAGCC-3'. The primers used for *DEPDC1* isoform-specific qPCR analysis were: *DEPDC1* all forward, 5'-TGATGCAATGGGTACGAGGT-3'; reverse, 5'-TCTTCCAGCAAGAAGCTCATCA-3'; *DEPDC1* long isoform forward, 5'-GAACTCGGAGAGTCTAGTGCC-3'; reverse, 5'-CATGATGGCAACCCCTCTCT-3'. The efficiency of *UPF1* knockdown was measured at the mRNA level by RT-qPCR: forward, 5'-AATTTGGTTAAGAGACATGCGG-3'; reverse, 5'-TCAGGGACCTTGATGACGTG-3'.

Mitophagy measurement and fluorescence microscopy. WT and *SRSF2*^{P95H/+} K562 cells were treated with DMSO or 3 μM CHIR for 44 hours, then seeded on poly-D-lysine-coated slides for 4 hours at 37°C. After incubation, cells were fixed with 4% paraformaldehyde (pH 7.4) for 15 minutes, permeabilized with 0.1% Triton X-100 for 15 minutes, and blocked with 2% BSA in PBS for 1 hour at room temperature. Cells were immunostained with mouse anti-TOMM20 antibody (1:100 dilution; clone 4F3, Sigma-Aldrich, WH0009804M1) and rabbit anti-LAMP1 antibody (1:100 dilution; ABclonal A2582) overnight at 4°C in a humidified chamber. Cells were incubated with secondary anti-rabbit AF568 (Invitrogen A11011) and anti-mouse AF488 (1:1,000 dilution; Invitrogen, A11001) antibodies at room temperature for 60 minutes. The slides were then air-dried in the dark at room temperature for 10 minutes and mounted in Anti-Fade mounting medium (Abcam ab104135) before confocal imaging. Colocalization of TOMM20 and LAMP1 was quantified with the JaCoP plug-in in Fiji. Flux analysis was performed to quantify the turnover of mitochondria in lysosomes by evaluating the accumulation of mitochondria in the presence of the lysosomal inhibitors (31). Cells were cultured in the presence or absence of 100 μM CQ or 50 μM Lys05 for 4 hours, and then cells were subjected to MitoTracker green (MTG) (Invitrogen, M7514) staining for flow cytometric analysis. Mitophagic flux was determined by subtraction of the MTG value for untreated cells from the value for cells treated with either CQ or Lys05 (31, 40).

For PINK1 staining, cells were immunostained with rabbit anti-PINK1 antibody (1:100 dilution; Proteintech 23274-1-AP), mouse anti-TOMM20 antibody (1:200 dilution), and mouse anti-PARKIN antibody (1:100 dilution; Proteintech 66674-1-1g) as previously described. For high-resolution imaging, the stained slides were imaged using a Zeiss LSM880 confocal microscope with Airyscan. Images were captured using a ×60 objective with Z-stacks followed by deconvolution analysis.

Measurements of mitochondrial mass, membrane potential, ROS, and mitochondrial DNA copy number. For mitochondrial mass measurement, cells were stained with 15 nM MTG for 20 minutes at room temperature in the dark followed by flow cytometric analysis. For mitochondrial membrane potential analysis, cells were stained with 200 nM TMRE (Invitrogen, T669) for 20 minutes at room temperature. JC-1 (Invitrogen, M34152) staining was used to detect mitochondrial depolarization occurring in apoptosis.

WT and *SRSF2*^{P95H/+} K562 cells were treated with or without 2 μM CCCP for 24 hours, and then stained with 1 μM JC-1 for 20 minutes. Cellular ROS levels were measured by FACS following cell surface staining using the CellROX kit (Invitrogen, C10444) according to the manufacturer's instructions. To quantify mitochondrial DNA copy number, qPCR was performed with primers for mitochondrial mt-ND1 (forward, GCAGAGACCAACCGAACCCCC; reverse, GGGCCTGCGGCGTATTTCGAT) and nuclear β₂-microglobulin (B2M) (forward, GCAGAGACCAACCGAACCCCC; reverse, GGC-GGGCCACCAAGGAGAAC).

Transmission electron microscopy. K562 WT and *SRSF2*^{P95H/+} cells for electron microscopic examination were fixed with 2.5% glutaraldehyde, 2.0% paraformaldehyde in 0.1 M sodium cacodylate buffer (pH 7.4) overnight at 4°C. After subsequent buffer washes, the samples were postfixed in 2.0% osmium tetroxide for 1 hour at room temperature and rinsed in dH₂O before en bloc staining with 2% uranyl acetate. After dehydration through a graded ethanol series, the tissue was infiltrated and embedded in EMBED-812 (Electron Microscopy Sciences). Thin sections were stained with uranyl acetate and lead citrate and examined with a JEOL 1010 electron microscope fitted with a Hamamatsu digital camera and AMT Advantage image capture software. Images of single cells were saved as separate image files, and an observer blind to the identity of each cell counted vesicles per cell.

Measurement of mitochondrial respiration. Oxygen consumption was measured using high-resolution respirometry Oxygraph-2k (Oroboros Instruments) with a polarographic oxygen electrode and two 2-mL chambers allowing for parallel measurements. Briefly, K562 WT and *SRSF2*^{P95H/+} cells in MiRO5 buffer (0.5 mM EGTA, 3 mM MgCl₂, 60 mM lactobionic acid, 20 mM taurine, 10 mM KH₂PO₄, 20 mM HEPES, 110 mM D-sucrose, 1 g/L BSA) were added into the closed chamber through a small capillary tube. Oxygen concentration (μmol/L) and oxygen flux [pmol/(s·10⁶ cells)] were simultaneously recorded in real time. During the assay, 5 μg/mL digitonin, 5 mM pyruvate, 2 mM malate, 10 mM glutamate, 2.5 mM ADP, 5 nM oligomycin, 0.5 μM FCCP, 0.5 μM rotenone, and 2.5 μM antimycin A were added sequentially.

K562 xenograft model. K562 WT or *SRSF2*^{P95H/+} cells (5 × 10⁶) were subcutaneously implanted into the flank of female NSG mice of 6–8 weeks of age. Mice were then treated with 30 mg/kg body weight CHIR or vehicle (10% DMSO, 45% PEG400, and 45% PBS, injected subcutaneously) daily for the duration of the implantation period. Tumor size was measured 3 times a week using a caliper. Tumor volume was calculated by the ellipsoid formula: (length × width²)/2.

RNA-Seq sample preparation. K562 isogenic lines were treated with 3 μM CHIR for 24 hours. After treatment, the cells were washed with cold PBS, and RNA was isolated using an RNeasy Kit (QIAGEN) according to the manufacturer's instructions. cDNA library preparation, sequencing, and raw read filtering methods were described previously (22).

Quantification of RNA-Seq data. Raw sequence reads (10⁸ reads per replicate sample) were aligned to the human reference sequence hg38 by STAR 2.4.2a using 2-pass alignment. Raw gene counts were compiled into total gene counts, then analyzed using edgeR 3.20.2 to assess the significance of changes between cohorts. Gene changes with an adjusted *P* value less than 0.05 were considered significant. Significant gene expression changes are provided

in Supplemental Table 2. Heatmaps for BCL2 family gene expression and mitophagy-related gene expression were generated using the Morpheus tool (Broad Institute, <https://software.broadinstitute.org/morpheus/>). Briefly, normalized expression values were transformed to z -scored \log_2 expression by subtraction of row mean and then division by row standard deviation. RNA-Seq data were deposited in GEO (GSE235600) and are accessible as described below.

Identification of differential splicing events. Alternative splicing analyses relied on RNA-Seq reads mapped to the reference human genome as described using rMATS v4.1.1 with the default parameters (28). Events were defined as significant if (a) the FDR-corrected P value was smaller than 0.05 and (b) the dPSI was larger than 10%. Examples of splicing and mis-splicing events were visualized with the Integrative Genomics Viewer (Broad Institute). The heatmap for alternative splicing events between WT and *SRSF2*^{P95H/+} cells was generated by Morpheus. Hierarchical clustering was performed using metric one minus Pearson's correlation.

Gene Ontology analysis. Gene Ontology analysis was performed with Metascape (<https://metascape.org>) using the Kyoto Encyclopedia of Genes and Genomes (KEGG) and GO-specific signatures according to the manual.

GSEA analysis. GSEA was performed using GSEA version 4.3 (Broad Institute). Normalized read values produced from gene expression analysis were formatted into GCT files containing expression values for genes in different biological states. CLS files were manually built to label biological states involved in each study. The following parameters were used: number of permutations = 1,000, permutation type = gene_set, ChIP platform = human_Ensembl_gene_ID_MSigDB.v2023.1.chip. Other parameters were used at default values.

Mass spectrometry. *SRSF2*^{+/+} (WT) and *SRSF2*^{P95H/+} K562 cell pellets were resuspended in a solution of 100 mM ammonium bicarbonate and 8 M urea. Samples were sonicated for 15 seconds, then placed on ice for 15 seconds 10 times, and then were centrifuged at 20,000g for 5 minutes at 4°C. Protein concentration in supernatants was measured by bicinchoninic acid assay. For each sample, 100 µg of protein was diluted to 50 µL at a final concentration of 10 mM DTT and incubated at 56°C for 30 minutes to reduce cystines to cysteines. Alkylation was performed by addition of 5.5 µL of 0.5 M iodoacetamide and incubation at room temperature in the dark for 40 minutes. Samples were diluted to 250 µL with 50 mM Tris-HCl (pH 8.3), 2 µg of sequencing-grade modified trypsin (Promega) was added, and samples were incubated at 37°C overnight. Samples were acidified to 0.1% trifluoroacetic acid and immediately desalted using C18 StageTips (Thermo Fisher Scientific, 13-110-018), washed with 0.1% formic acid, and eluted with 0.1% formic acid in 60% acetonitrile. Peptides were dried in a Savant SpeedVac and then resuspended in 20 µL of 0.1% trifluoroacetic acid. UV absorption at 280 nm (A280) was measured to normalize injection volumes, and samples were run on a Dionex UltiMate 3000 nanoLC and Q Exactive HF (Thermo Fisher Scientific). Peptides were loaded on a C18 trap column (Thermo Fisher Scientific), washed with buffer A (0.1% formic acid), and then separated using an analytical column (75 µm × 15 cm) packed in-house with C18 resin (Dr. Maisch GmbH), using an analytical gradient of 5% buffer B (0.1% formic acid in 80% acetonitrile) to 25% over 90 minutes, and then 25% to 45% over 30 minutes. Mass spectrometric detection was performed using data-independent acquisition with 24 m/z windows. Data were searched using DIA-NN

(<https://github.com/vdemichev/DiaNN>) with a UniProt FASTA digest library-free search and without heuristic protein inference. The mass spectrometry proteomics data were deposited to the ProteomeXchange Consortium via the PRIDE (56) partner repository with the data set identifier PXD043213.

AML TCGA analysis. Gene expression analysis of *OPTN*, *ULK1*, and *TOMM7* in AML patients from the TCGA project (57) was retrieved from cBioPortal for Cancer Genomics (<https://www.cbioportal.org>) (58), and visualized using Prism (GraphPad). GEPIA (Gene Expression Profiling Interactive Analysis; <http://gepia.cancer-pku.cn>) was used for overall survival analysis based on high and low expression of *OPTN* in publicly available TCGA data sets.

Statistics. Statistical analysis was performed using Prism version 8 software. Statistical differences between 2 groups were determined by 2-tailed Student's t test. To assess the statistical significance of differences between more than 2 treatments, 1-way or 2-way ANOVA followed by Šidák's multiple-comparison test was used. P less than 0.05 was considered significant.

Study approval. All mouse studies were carried out through the Stem Cell and Xenograft Core under a protocol approved by the University of Pennsylvania Institutional Animal Care and Use Committee.

Data availability. RNA-Seq data were deposited in the NCBI's Gene Expression Omnibus (GEO) database (59) and are accessible through GEO Series accession number GSE235600 (<https://www.ncbi.nlm.nih.gov/geo/query/acc.cgi?acc=GSE235600>). The mass spectrometry proteomics data were deposited to the ProteomeXchange Consortium via the PRIDE (56) partner repository with the data set identifier PXD043213. Supporting data values for all figures are provided in the Supporting Data Values file.

Author contributions

XL and PSK conceptualized the study. XL, MQV, NS, MPC, RM, and KJ established methodology. PSK, OAW, KWL, and DCW supervised the study and acquired funding. XL, SAD, RFS, RM, KJ, MQV, OP, AAM, and CL performed investigation. PSK, RFS, OAW, NS, MPC, JH, KWL, and DCW provided resources. XL, PSK, RFS, RM, KJ, and NS wrote and/or edited the manuscript. XL, OP, and AAM performed visualization. PSK, OAW, KWL, DCW, MPC, and JH supervised the study. PSK and KWL acquired funding.

Acknowledgments

We appreciate helpful suggestions from M. Celeste Simon, Brian Keith, and Vikram Paralkar. We also thank Akmal Salimov for assistance with Stem Cell and Xenograft Core sample characterization, and Blake Hernandez for suggestions regarding confocal imaging. This research was supported by grants to PSK from the NIH (R01HL141759 and R56DK133258), the Leukemia and Lymphoma Society (8036-23), and the Institute for Translational Medicine and Applied Therapeutics at the University of Pennsylvania; to KWL from the NIH (R35GM118048); and to MPC from a Veterans Administration Merit Award (I01BX004662).

Address correspondence to: Peter S. Klein, 9-103 Smilow, Perelman School of Medicine at the University of Pennsylvania, 3400 Civic Center Boulevard, Philadelphia, Pennsylvania 19104, USA. Phone: 215.898.2179; Email: pklein@penndmedicine.upenn.edu.

1. Kim YJ, Abdel-Wahab O. Therapeutic targeting of RNA splicing in myelodysplasia. *Semin Hematol.* 2017;54(3):167–173.
2. Dvinge H, et al. RNA splicing factors as oncoproteins and tumour suppressors. *Nat Rev Cancer.* 2016;16(7):413–430.
3. Yoshida K, et al. Frequent pathway mutations of splicing machinery in myelodysplasia. *Nature.* 2011;478(7367):64–69.
4. Papaemmanuil E, et al. Somatic SF3B1 mutation in myelodysplasia with ring sideroblasts. *N Engl J Med.* 2011;365(15):1384–1395.
5. Graubert TA, et al. Recurrent mutations in the U2AF1 splicing factor in myelodysplastic syndromes. *Nat Genet.* 2011;44(1):53–57.
6. Inoue D, et al. Spliceosomal gene mutations in myelodysplasia: molecular links to clonal abnormalities of hematopoiesis. *Genes Dev.* 2016;30(9):989–1001.
7. Kim E, et al. SRSF2 mutations contribute to myelodysplasia by mutant-specific effects on exon recognition. *Cancer Cell.* 2015;27(5):617–630.
8. Rivera OD, et al. Alternative splicing redefines landscape of commonly mutated genes in acute myeloid leukemia. *Proc Natl Acad Sci U S A.* 2021;118(15):e2014967118.
9. Pellagatti A, et al. Impact of spliceosome mutations on RNA splicing in myelodysplasia: dysregulated genes/pathways and clinical associations. *Blood.* 2018;132(12):1225–1240.
10. Bejar R, et al. Validation of a prognostic model and the impact of mutations in patients with lower-risk myelodysplastic syndromes. *J Clin Oncol.* 2012;30(27):3376–3382.
11. Patnaik MM, Tefferi A. Cytogenetic and molecular abnormalities in chronic myelomonocytic leukemia. *Blood Cancer J.* 2016;6(2):e393.
12. Lee SC, et al. Modulation of splicing catalysis for therapeutic targeting of leukemia with mutations in genes encoding spliceosomal proteins. *Nat Med.* 2016;22(6):672–678.
13. Wang E, et al. Targeting an RNA-binding protein network in acute myeloid leukemia. *Cancer Cell.* 2019;35(3):369–384.
14. Steensma DP, et al. Phase I first-in-human dose escalation study of the oral SF3B1 modulator H3B-8800 in myeloid neoplasms. *Leukemia.* 2021;35(12):3542–3550.
15. Hsu TY, et al. The spliceosome is a therapeutic vulnerability in MYC-driven cancer. *Nature.* 2015;525(7569):384–388.
16. Crews LA, et al. RNA splicing modulation selectively impairs leukemia stem cell maintenance in secondary human AML. *Cell Stem Cell.* 2016;19(5):599–612.
17. Shirai CL, et al. Preclinical activity of splicing modulators in U2AF1 mutant MDS/AML. *Blood.* 2015;126(23):1653.
18. Seiler M, et al. H3B-8800, an orally available small-molecule splicing modulator, induces lethality in spliceosome-mutant cancers. *Nat Med.* 2018;24(4):497–504.
19. Liu X, Klein PS. Glycogen synthase kinase-3 and alternative splicing. *Wiley Interdiscip Rev RNA.* 2018;9(6):e1501.
20. Huang J, et al. Pivotal role for glycogen synthase kinase-3 in hematopoietic stem cell homeostasis in mice. *J Clin Invest.* 2009;119(12):3519–3529.
21. Guezguez B, et al. GSK3 deficiencies in hematopoietic stem cells initiate pre-neoplastic state that is predictive of clinical outcomes of human acute leukemia. *Cancer Cell.* 2016;29(1):61–74.
22. Shinde MY, et al. Phosphoproteomics reveals that glycogen synthase kinase-3 phosphorylates multiple splicing factors and is associated with alternative splicing. *J Biol Chem.* 2017;292(44):18240–18255.
23. Heyd F, Lynch KW. Phosphorylation-dependent regulation of PSF by GSK3 controls CD45 alternative splicing. *Mol Cell.* 2010;40(1):126–137.
24. Hernandez F, et al. Glycogen synthase kinase-3 plays a crucial role in tau exon 10 splicing and intranuclear distribution of SC35. Implications for Alzheimer's disease. *J Biol Chem.* 2004;279(5):3801–3806.
25. Wang SB, et al. Protein S-nitrosylation controls glycogen synthase kinase 3 β function independent of its phosphorylation state. *Circ Res.* 2018;122(11):1517–1531.
26. Martinez NM, et al. Widespread JNK-dependent alternative splicing induces a positive feedback loop through CELF2-mediated regulation of MKK7 during T-cell activation. *Genes Dev.* 2015;29(19):2054–2066.
27. Lee SC, et al. Synthetic lethal and convergent biological effects of cancer-associated spliceosomal gene mutations. *Cancer Cell.* 2018;34(2):225–241.
28. Shen S, et al. rMATS: robust and flexible detection of differential alternative splicing from replicate RNA-Seq data. *Proc Natl Acad Sci U S A.* 2014;111(51):E5593–E5601.
29. Darman RB, et al. Cancer-associated SF3B1 hotspot mutations induce cryptic 3' splice site selection through use of a different branch point. *Cell Rep.* 2015;13(5):1033–1045.
30. Lazarou M, et al. The ubiquitin kinase PINK1 recruits autophagy receptors to induce mitophagy. *Nature.* 2015;524(7565):309–314.
31. Mauro-Lizcano M, et al. New method to assess mitophagy flux by flow cytometry. *Autophagy.* 2015;11(5):833–843.
32. Yoshimi A, et al. Coordinated alterations in RNA splicing and epigenetic regulation drive leukemogenesis. *Nature.* 2019;574(7777):273–277.
33. Salvioli S, et al. JC-1, but not DiOC6(3) or rhodamine 123, is a reliable fluorescent probe to assess delta psi changes in intact cells: implications for studies on mitochondrial functionality during apoptosis. *FEBS Lett.* 1997;411(1):77–82.
34. Ito K, et al. Self-renewal of a purified Tie2+ hematopoietic stem cell population relies on mitochondrial clearance. *Science.* 2016;354(6316):1156–1160.
35. Ayyathan DM, et al. Inhibition of PINK1-dependent mitochondrial quality control pathways induces senescence of acute myeloid leukemia stem cells. *Blood.* 2021;138:2225.
36. Pei S, et al. AMPK/FIS1-mediated mitophagy is required for self-renewal of human AML stem cells. *Cell Stem Cell.* 2018;23(1):86–100.
37. Juhaszova M, et al. Glycogen synthase kinase-3 β mediates convergence of protection signaling to inhibit the mitochondrial permeability transition pore. *J Clin Invest.* 2004;113(11):1535–1549.
38. Nguyen-McCarty M, Klein PS. Autophagy is a signature of a signaling network that maintains hematopoietic stem cells. *PLoS One.* 2017;12(5):e0177054.
39. McAfee Q, et al. Autophagy inhibitor Lys05 has single-agent antitumor activity and reproduces the phenotype of a genetic autophagy deficiency. *Proc Natl Acad Sci U S A.* 2012;109(21):8253–8258.
40. Dykstra KM, et al. Inhibiting autophagy targets human leukemic stem cells and hypoxic AML blasts by disrupting mitochondrial homeostasis. *Blood Adv.* 2021;5(8):2087–2100.
41. Mossner M, et al. Mutational hierarchies in myelodysplastic syndromes dynamically adapt and evolve upon therapy response and failure. *Blood.* 2016;128(9):1246–1259.
42. Cancer Genome Atlas Research Network, et al. Genomic and epigenomic landscapes of adult de novo acute myeloid leukemia. *N Engl J Med.* 2013;368(22):2059–2074.
43. Vannini N, et al. The NAD-booster nicotinamide riboside potentially stimulates hematopoiesis through increased mitochondrial clearance. *Cell Stem Cell.* 2019;24(3):405–418.
44. Nasr W, Filippi MD. Acquired and hereditary bone marrow failure: a mitochondrial perspective. *Front Oncol.* 2022;12:1048746.
45. Mattes K, et al. Differential redox-regulation and mitochondrial dynamics in normal and leukemic hematopoietic stem cells: a potential window for leukemia therapy. *Crit Rev Oncol Hematol.* 2019;144:102814.
46. Glytsou C, et al. Mitophagy promotes resistance to BH3 mimetics in acute myeloid leukemia. *Cancer Discov.* 2023;13(7):1656–1677.
47. Chen X, et al. Targeting mitochondrial structure sensitizes acute myeloid leukemia to venetoclax treatment. *Cancer Discov.* 2019;9(7):890–909.
48. Nechiporuk T, et al. The TP53 apoptotic network is a primary mediator of resistance to BCL2 inhibition in AML Cells. *Cancer Discov.* 2019;9(7):910–925.
49. Ong F, et al. Venetoclax resistance: mechanistic insights and future strategies. *Cancer Drug Resist.* 2022;5(2):380–400.
50. Durcan TM, Fon EA. The three 'P's of mitophagy: PARKIN, PINK1, and post-translational modifications. *Genes Dev.* 2015;29(10):989–999.
51. Liu X, et al. Targeting the coronavirus nucleocapsid protein through GSK-3 inhibition. *Proc Natl Acad Sci U S A.* 2021;118(42):e2113401118.
52. Bourhill T, et al. Enzastaurin: a lesson in drug development. *Crit Rev Oncol Hematol.* 2017;112:72–79.
53. Sanchez-Cruz A, et al. GSK-3 inhibitors: from the brain to the retina and back again. *Adv Exp Med Biol.* 2019;1185:437–441.
54. Odia Y, et al. Malignant glioma subset from actuate 1801: phase I/II study of 9-ING-41, GSK-3 β inhibitor, monotherapy or combined with chemotherapy for refractory malignancies. *Neurooncol Adv.* 2022;4(1):vdac012.
55. Hou P, et al. Genome editing of CXCR4 by CRISPR/cas9 confers cells resistant to HIV-1 infection. *Sci Rep.* 2015;5:15577.
56. Perez-Riverol Y, et al. The PRIDE database resources in 2022: a hub for mass spectrometry-based proteomics evidences. *Nucleic Acids*

- Res.* 2022;50(d1):D543–D552.
57. Tyner JW, et al. Functional genomic landscape of acute myeloid leukaemia. *Nature*. 2018;562(7728):526–531.
58. Cerami E, et al. The cBio cancer genomics portal: an open platform for exploring multidimensional cancer genomics data. *Cancer Discov*. 2012;2(5):401–404.
59. Edgar R, et al. Gene Expression Omnibus: NCBI gene expression and hybridization array data repository. *Nucleic Acids Res*. 2002;30(1):207–210.